Doklady Physics, Vol. 48, No. 2, 2003, pp. 57–61. Translated from Doklady Akademii Nauk, Vol. 388, No. 4, 2003, pp. 466–471.

PHYSICS

Excitation of Low-Lying Lead Atomic Levels in Electron–Atom and Electron–Molecule Collisions

Yu. M. Smirnov

Presented by Academician F.B. Bunkin September 12, 2002

Received September 27, 2002

1. Lasing on transitions from a resonance level to a metastable level is of considerable interest, because it can provide very high efficiency. Lasing on such transitions in a Pb atom was first obtained at the initial stage of investigations [1]. Later, the number of lasing transitions in the Pb atom was significantly increased [2]. However, all the new generation lines corresponded to transitions of the same type as the initial 722.897-nm line. The operating temperature of a discharge tube was sustained in the range 850–1000°C, while the pressure of lead vapors reached a value of 0.1 Torr, which is characteristic for gas-discharge lasers, even for temperature $t(0.1) = 837$°C.

The use of lead halides as a working medium for lasers made it possible to significantly reduce the necessary temperature of the discharge tube to 420–560°C [3] and to about 570°C [4]. Lead dichloride was used as the initial substance in both studies. In [5], lead dibromide was used and lasing was obtained for 722.897- and 406.214-nm PbI lines. The temperature of the discharge tube was equal to 400–500°C, and lead dibromide was formed in the reaction of metallic-lead inserts with an HBr vapor flow.

All lasers based on the lead atomic transition operate in the mode of excitation by short pulses with a high repetition frequency. Chen [3] used the double-pulse technique, while Kazaryan and Trofimov [4] obtained generation in the excitation mode with regular pulses. In the double-pulse mode, the first pulse is used to dissociate initial halide molecules, whereas the second pulse is directly used to excite lead atoms formed at the first stage. Bokhan and Sorokin [6] showed that, for a lead-vapor laser, pumping by an electron beam with an energy of several keV is much more efficient than that by an electric discharge. Alternative pumping methods can be discussed in principle also for halide-vapor lasers, because dissociative excitation gives rise to the production of a certain portion of lead atoms immediately in excited states. However, this process has not yet been studied, which hinders the estimation of the possibility of its use.

The efficiency of the excitation of lead atoms in electron–atom collisions is poorly studied. Inelastic collisions of 50- and 150-eV electrons with lead atoms were experimentally investigated in [7], where 24 cross sections for the excitation of PbI spectral lines, as well as 7 optical excitation functions, were measured. Using the Born approximation, Peterkop [8] calculated eight cross sections for the excitation of the spectral lines of a lead atom, including six cross sections earlier measured in [7]. This calculation underestimated experimental data for an electron energy of 50 eV by a factor of 7–15. Comparing the calculated and experimental oscillator strengths and taking into account the Bethe formula, Peterkop [8] concluded that the calculated cross sections were more correct than the values measured in [7]. The other experimental data [9] were published almost simultaneously with work [8]. However, Peterkop [8] became aware of these results only after the publication of his paper.

This paper is devoted to the dissociative excitation of lead atoms in e–$PbCl_2$ collisions. Refined data on the cross sections for the excitation of lead atoms in electron–atom collisions are obtained. Only transitions between low-lying levels are studied, which are of interest for further development of lasers based on both lead vapors and its halides.

2. The method of extended crossing beams with the detection of an optical signal of excited particles from the region of beam crossing is used. The features of the experimental procedure with extended crossing beams have been repeatedly discussed [10, 11].

In an experiment with $PbCl_2$, the substance under investigation evaporated from a tantalum crucible heated by a defocused electron beam. At a crucible temperature of 750 K, the molecule density in the region of the crossing of electron and molecular beams reaches 3.4×10^{11} cm^{-3}. A $PbCl_2$ molecule corresponds to the C_{2v} point symmetry group with angle $\angle ClPbCl = 96° \pm 3°$ and has three fundamental vibrational frequencies $\nu_1 = 314$ cm^{-1}, $\nu_2 = 99$ cm^{-1}, and $\nu_3 = 299$ cm^{-1} [12]. The evaporation of molecules is accompanied by the popu-

Moscow Power Engineering Institute (Technical University), ul. Krasnokazarmennaya 14, Moscow, 111250 Russia

1028-3358/03/4802-0057$24.00

Table 1. Cross sections for the excitation of the lead atom

λ, nm	Transition	*J*	E_{low}, cm^{-1}	E_{up}, cm^{-1}	*Q*, 10^{-18} cm^2		Q_{max}, 10^{-18} cm^2		$E(Q_{max})$, eV		*OEF*
					Pb (50)	$PbCl_2$ (100)	Pb	$PbCl_2$	Pb	$PbCl_2$	
202.202	$6p^2(1/2, 1/2)–6p7s(3/2, 1/2)°$	0–1	0	49439							
217.000	$6p^2(1/2, 1/2)–6p6d1/2[3/2]°$	0–1	0	46068	27.2	–	63.1	–	8.6	–	5
240.194	$6p^2(3/2, 1/2)–6p7s(3/2, 1/2)°$	1–1	7819	49439	0.52	–	0.74	–	9.0	–	3
247.638	$6p^2(3/2, 1/2)–6p7s(3/2, 1/2)°$	1–2	7819	48188	0.45	–	1.50	–	10	–	4
257.726	$6p^2(3/2, 1/2)–6p7s(3/2, 1/2)°$	2–1	10650	49439	1.20	0.38	1.71	0.44	9.0	68	3
261.365	$6p^2(3/2, 1/2)–6p6d1/2[3/2]°$	1–1	7819	46068	21.5	0.44	50.0	–	8.6	–	5
261.417	$6p^2(3/2, 1/2)–6p6d1/2[3/2]°$	1–2	7819	46060							
265.709	$6p^2(3/2, 1/2)–6p6d1/2[5/2]°$	1–2	7819	45443							
266.315	$6p^2(3/2, 1/2)–6p7s(3/2, 1/2)°$	2–2	10650	48188	1.10	0.49	3.66	0.57	10	70	4
280.200	$6p^2(3/2, 1/2)–6p6d1/2[5/2]°$	2–3	10650	46328	8.22	0.84	21.0	–	8.6	–	7
282.258	$6p^2(3/2, 1/2)–6p6d1/2[3/2]°$	2–1	10650	46068	0.32	–	0.74	–	8.6	–	5
282.319	$6p^2(3/2, 1/2)–6p6d1/2[3/2]°$	2–2	10650	46060							
283.305	$6p^2(1/2, 1/2)–6p7s(1/2, 1/2)°$	0–1	0	35287	46.9	5.26	61.7	5.56	18	65	2
287.332	$6p^2(3/2, 1/2)–6p6d1/2[5/2]°$	2–2	10650	45443	3.73	0.63	18.5	–	9.0	–	6
357.273	$6p^2(3/2, 3/2)–6p7s(3/2, 1/2)°$	2–1	21457	49439	1.82	0.55	2.60	0.63	9.0	68	3
363.957	$6p^2(3/2, 1/2)–6p7s(1/2, 1/2)°$	1–1	7819	35287	30.3	3.39	39.8	3.59	18	65	2
368.346	$6p^2(3/2, 1/2)–6p7s(1/2, 1/2)°$	1–0	7819	34959	5.52	5.62	24.5	5.76	8.0	90	1
373.994	$6p^2(3/2, 3/2)–6p7s(3/2, 1/2)°$	2–2	21457	48188	1.21	0.64	4.03	0.75	10	70	4
401.963	$6p^2(3/2, 3/2)–6p6d1/2[5/2]°$	2–3	21457	46328	0.45	0.056	1.15	–	8.6	–	7
405.781	$6p^2(3/2, 1/2)–6p7s(1/2, 1/2)°$	2–1	10650	35287	115.0	14.7	151.	15.5	18	65	2
406.214	$6p^2(3/2, 3/2)–6p6d1/2[3/2]°$	2–1	21457	46068	17.4	0.35	40.5	–	8.6	–	5
416.803	$6p^2(3/2, 3/2)–6p6d1/2[5/2]°$	2–2	21457	45443	0.31	0.054	1.54	–	9.0	–	6
500.542	$6p^2(3/2, 3/2)–6p7s(3/2, 1/2)°$	0–1	29466	49439	0.61	0.16*	0.87	0.19	9.0	68	3
602.185	$6p^2(3/2, 3/2)–6p6d1/2[3/2]°$	0–1	29466	46068							
722.897	$6p^2(3/2, 3/2)–6p7s(1/2, 1/2)°$	2–1	21457	35287	3.43	0.39	4.52	0.41	18	65	2

lation of low-lying vibration–rotation levels of the ground electron state of the molecule due to thermal excitation. Celiberto *et al.* [13] showed theoretically that the cross sections for the dissociative excitation of H_2 and D_2 molecules depend significantly on the initial vibrational level.

For molecules, including $PbCl_2$, other than those mentioned above, any quantitative information on the effect of the initial vibrational excitation on cross sections is absent. In the case under consideration, the distribution of molecules over the ν_2-vibration levels is wide, and no level dominates. On the contrary, narrow distributions correspond to ν_1 and ν_3 vibrations: about 84% of beam molecules are on three low levels with vibrational quantum numbers $v \le 2$ for both cases. The redistribution of molecules over the levels of ν_1 and ν_3 vibrations with varying temperature noticeably changes the resulting cross sections for dissociative excitation, and this effect must be taken into account when comparing experimental results with future theory.

The remaining experimental conditions were not specific for $PbCl_2$ and were presented in [9, 11].

3. For wavelengths of 210–760 nm, about 160 spectral lines arising due to the bombardment of $PbCl_2$ molecules by a monoenergetic 100-eV electron beam were observed. These lines are attributed to the spectra of the lead atom and singly charged lead ion. The spectral bands of the PbCl molecule were not observed.

The results concerning the excitation of the low-lying levels of the lead atom, along with the necessary spectroscopic information, are presented in Table 1. This table includes the wavelength λ; transition and

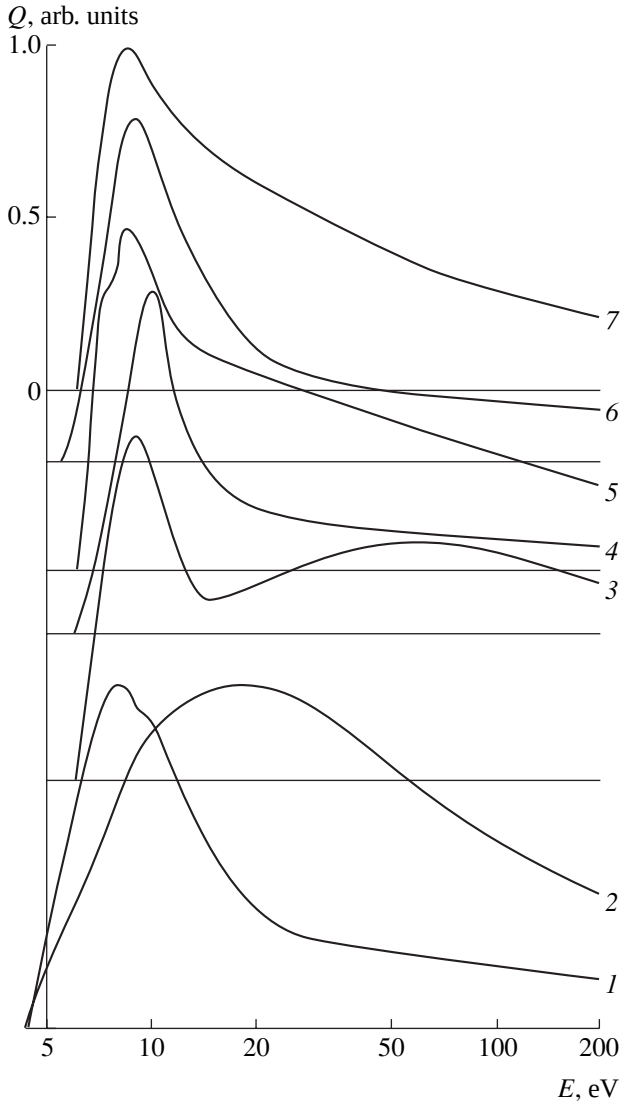

Fig. 1. Optical excitation functions of the spectral lines of the lead atom in e–Pb collisions. The abscissa axis is logarithmic, whereas the ordinate axis is linear with an individual zero for each line. All the lines are normalized to unity at the maximum.

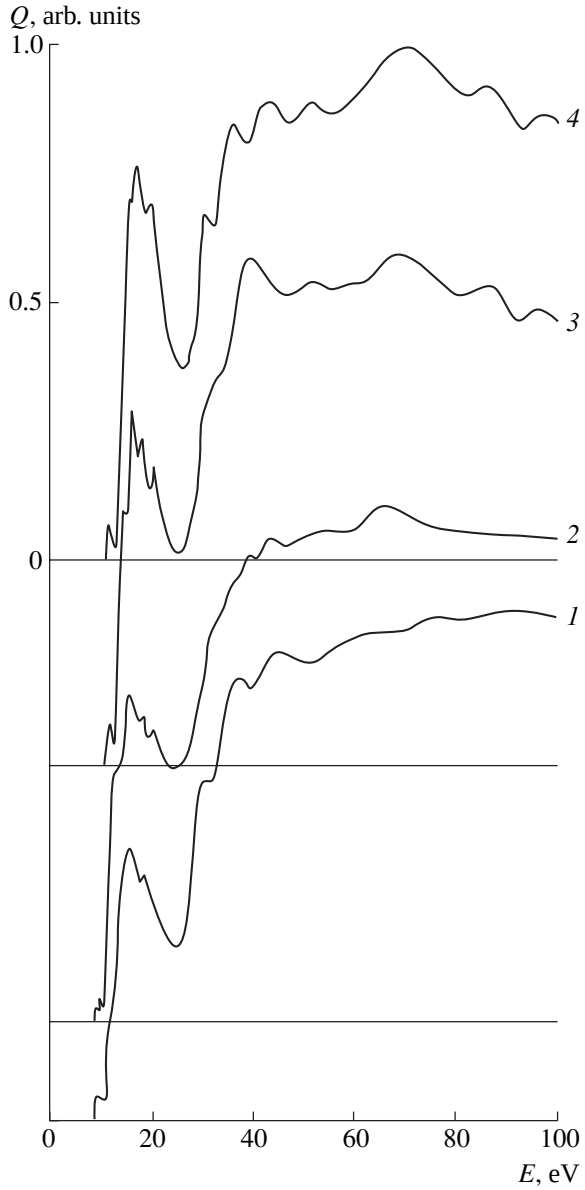

Fig. 2. Optical excitation functions of the spectral lines of the lead atom in e–$PbCl_2$ collisions. Both axes are linear.

internal quantum number J according to [14]; energies of the lower and upper levels measured from the ground state of the lead atom; cross sections Q for an energy of 50 and 100 eV for e–Pb and e–$PbCl_2$ collisions, respectively; cross sections Q_{max} at the maximum of the optical excitation function; the position of the maximum $E(Q_{max})$; and the optical excitation function number corresponding to the numbering of the lines in Figs. 1 and 2. We note that the numberings of the optical excitation function of a particular transition for direct and dissociative excitations coincide with each other. The cross section for the dissociative excitation of the 500.542-nm line was obtained by separating the possible contribution from the 500.657-nm line and is marked by an asterisk in Table 1. Table 1 includes all the PbI transitions occurring in the group of levels under consideration according to available spectroscopic data [14], three of which—202.202, 265.709, and 602.185 nm—were observed in neither direct nor dissociative excitation, because the cross sections for their excitation are small.

The scheme of the PbI levels under consideration, together with all the known transitions, is shown in Fig. 3. The dashed lines are the three above-mentioned levels that were not detected in this work, double lines are laser transitions, and dash–dotted lines are five transitions that were observed in direct excitation but were not detected in e–$PbCl_2$ collisions, because the cross sections for direct excitation are much larger than the cross sections for dissociative excitation. All the terms

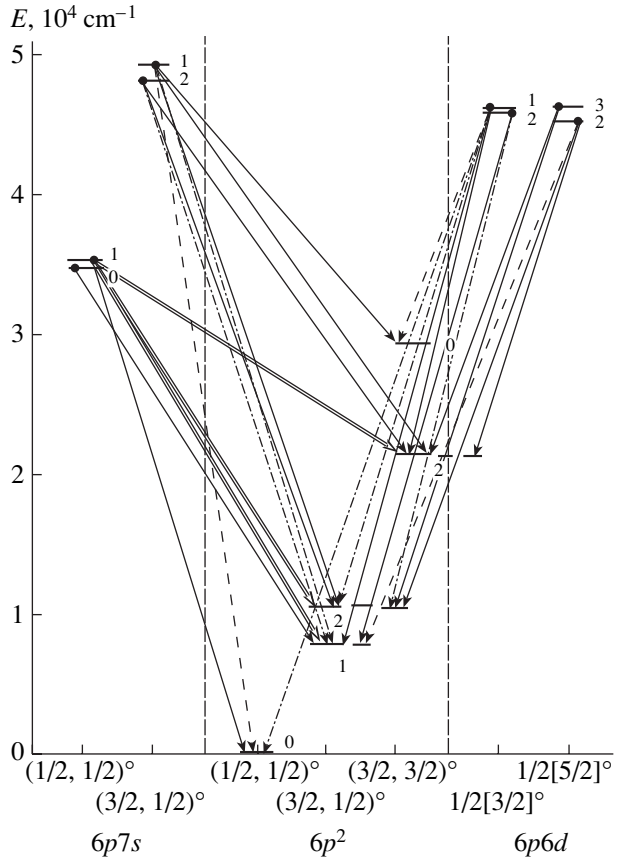

Fig. 3. Scheme of low-lying levels of the lead atom. The double lines are laser transitions, dashed lines are transitions that were not observed in this study, and dash–dotted lines are transitions studied only in electron–atom collisions.

below 30000 cm^{-1} are associated with the $6p^2$ configuration and are even. For this reason, the probabilities of transitions between these terms are very low even in the lead atom [15]. The number of possible resonance transitions in the group of terms under consideration is small, because the PbI $6p^2(1/2, 1/2)°$ ground state has $J = 0$ and transitions to it are possible only from odd levels with $J = 1$.

Table 1 shows that the cross sections for the dissociative excitation of the PbI transitions under study are systematically smaller than the cross sections for direct excitation by a factor of 2 to 50. This difference is larger for transitions from *d* levels. The only exclusion is the 368.346-nm level, for which Q(Pb, 50) virtually coincides with $Q(PbCl_2, 100)$. However, Q_{max} values differ by a factor of more than 4 even for this line, because its optical excitation function for direct excitation has a narrow maximum and decreases considerably to 50 eV. For dissociative excitation, the shapes of all the observed optical excitation functions differ only slightly from each other and the cross sections vary in a narrow range for an electron energy range of 35–100 eV. Comparison of the cross sections for direct excitation at an energy of 50 eV with the cross sections for dissociative excitation at an energy of 100 eV seems to be correct, because the threshold energies for these two processes differ by a factor of about 2 for the $PbCl_2$ molecule.

There are numerous channels of the formation of excited lead atoms in the collisions of 100-eV electrons with $PbCl_2$ molecules. The following reactions proceed for low energies (processes involving negative ions are omitted):

$$PbCl_2 + e \longrightarrow Pb^* + Cl_2 + e' \quad (9.22), \qquad (1)$$

$$\longrightarrow Pb^* + 2Cl + e' \quad (11.70), \qquad (2)$$

$$\longrightarrow Pb^* + Cl_2^* + e' \quad (\sim 11.7), \qquad (3)$$

$$\longrightarrow Pb^* + Cl_2^+ + e' + e'' \quad (20.70), \qquad (4)$$

$$\longrightarrow Pb^* + Cl + Cl^* + e' \quad (\sim 20.9), \qquad (5)$$

$$\longrightarrow Pb^* + Cl + Cl^+ + e' + e'' \quad (22.19), \qquad (6)$$

$$\longrightarrow Pb^* + Cl^{*'} + Cl^{*''} + e' \quad (\sim 30.1), \qquad (7)$$

where e and e' are the incident and scattered electrons, respectively; e'' is an electron knocked out of a chlorine atom or molecule when they are ionized; an asterisk means an excited particle; and the threshold appearance energies E_{app} in electron volts calculated disregarding the energy of thermal motion are given in parentheses. All the appearance energies are calculated for the most intense 405.781-nm line, for which this energy can be measured most accurately.

The measured value $E_{app} = 9.0 \pm 0.3$ eV agrees with the value calculated for reaction (1). However, this process contributes no more than 5% of Q_{max}. The optical excitation function begins to increase again at 11.5 ± 0.3 eV, and this increase is associated with contributions from reactions (2) and (3), among which reaction (2) seems to prevail. The total contribution from these reactions reaches 50%. A further significant increase in the optical excitation function begins near 24 eV and is likely attributed to the appearance of reaction (6). The origin of the optical excitation function structure for 15–20 eV is unclear. A detailed interpretation of the behavior of the optical excitation function can be based only on rigorous theoretical analysis.

As was mentioned above, data measured by Aleksakhin *et al.* [7] for the cross sections for excitation of the low-lying levels of the lead atom in the collisions of 50-eV electrons with lead atoms are one to two orders of magnitude larger than those calculated by Peterkop [8]. Table 2 presents these data and our results, which differ only slightly from the previous results [9]. As is seen, our results are systematically smaller than experimental data [7] by a factor of 6.7–11.8 (8.95 on average for six values). For the three most intense lines corresponding to transitions from the common upper $6p7s(1/2, 1/2)_1^\circ$ level, our experimental data differ from calculation [8] by 10–33%. For the two weaker lines, this difference is equal to a factor of 17 and 24, respectively. The cross sections calculated for other

Table 2. Cross sections for the excitation of the lead atom for an electron energy of 50 eV as obtained in various works

λ, nm	Upper level	Q_{50}, 10^{-18} cm^2		
		this study	[7]	[8]
240.194	$6p7s(3/2, 1/2)^\circ_1$	0.52	–	0.03
247.638	$6p7s(3/2, 1/2)^\circ_2$	0.45	–	0
257.726	$6p7s(3/2, 1/2)^\circ_1$	1.20	12.	0.05
266.315	$6p7s(3/2, 1/2)^\circ_2$	1.10	13.	0
283.305	$6p7s(1/2, 1/2)^\circ_1$	46.9	350.	52.4
363.957	$6p7s(1/2, 1/2)^\circ_1$	30.3	220.	23.7
368.346	$6p7s(1/2, 1/2)^\circ_0$	5.52	37	0
405.781	$6p7s(1/2, 1/2)^\circ_1$	115.	1200.	76.9

three lines in the Born approximation are equal to zero. According to these results, it is reasonable to restrict the application of the Born approximation to the most intense completely allowed transitions in such a complex electron shell as that of the lead atom.

4. The dissociative excitation of the lead atom in the collisions of electrons with $PbCl_2$ molecules was studied. The cross sections for dissociative excitation at intermediate energies (50–100 eV) are several times smaller than those for the excitation of the lead atom in e–Pb collisions. Experimental data on the cross sections for the direct excitation of intense lines agree well Born approximation calculations. Therefore, the previous discrepancy between calculated and measured cross sections by one to two orders of magnitude is removed. Acquired information can be used for the further development of gas lasers based on both lead vapor and $PbCl_2$ and for the theory of dissociative excitation.

REFERENCES

1. G. R. Fowles and W. T. Silfvast, Appl. Phys. Lett. **6** (4), 236 (1965).
2. A. A. Isaev and G. G. Petrash, Pis'ma Zh. Éksp. Teor. Fiz. **10** (1), 188 (1969) [JETP Lett. **10**, 119 (1969)].
3. C. J. Chen, J. Appl. Phys. **45** (10), 4663 (1974).
4. M. A. Kazaryan and A. N. Trofimov, Kratk. Soobshch. Fiz., No. 4, 33 (1976).
5. D. R. Jones and C. E. Little, IEEE J. Quantum Electron. **28** (3), 590 (1992).
6. P. A. Bokhan and A. R. Sorokin, Pis'ma Zh. Tekh. Fiz. **10** (10), 620 (1984) [Sov. Tech. Phys. Lett. **10**, 262 (1984)].
7. I. S. Aleksakhin, A. A. Borovik, V. P. Starodub, and I. I. Shafran'osh, Opt. Spektrosk. **46** (6), 1125 (1979) [Opt. Spectrosc. **46**, 636 (1979)].
8. R. K. Peterkop, Izv. Akad. Nauk Latv. SSR, Ser. Fiz. Tekh. Nauk, No. 2, 6 (1985).
9. P. A. Kolosov and Yu. M. Smirnov, *Elementary Processes in Atomic Collisions* (ChGU, Cheboksary, 1984), p. 58.
10. Yu. M. Smirnov, *Physics of Electron and Atomic Collisions* (Fiz. Tekh. Inst. Akad. Nauk SSSR, Leningrad, 1985), p. 183.
11. Yu. M. Smirnov, J. Phys. II (France) **4** (1), 23 (1994).
12. K. S. Krasnov, N. V. Filippenko, V. A. Bobkova, *et al.*, *Molecular Constants of Inorganic Compounds* (Khimiya, Leningrad, 1979).
13. R. Celiberto, U. T. Lamanna, and M. Capitelli, Phys. Rev. A **50**, 4778 (1994).
14. D. R. Wood and K. L. Andrew, J. Opt. Soc. Am. **58** (6), 818 (1968).
15. T. Gil and J. Heldt, Z. Phys. A **312** (4), 343 (1983).

Translated by R. Tyapaev

Doklady Physics, Vol. 48, No. 2, 2003, pp. 62–64. Translated from Doklady Akademii Nauk, Vol. 388, No. 5, 2003, pp. 608–610.

PHYSICS

Effect of Magneto-Induced Diffusion Instability in III–V Semiconductor Compounds

M. N. Levin*, G. V. Semenova, and T. P. Sushkova

Presented by Academician V.Ya. Shevchenko July 2, 2002

Received July 2, 2002

By now, there is much experimental evidence that relatively weak (<1 T) pulsed magnetic fields (PMFs) can uniquely act on the real structure and physical features of various diamagnetic crystals [1–5]. The effects induced by a magnetic field are attributed to the removal of exclusions for intercombination transitions of electrons involved in the formation of chemical bonds in complexes of defects with paramagnetic impurity centers [6]. The concepts of the spin nature of magnetic action, which were first developed in the theory of radical reactions in liquid media [7], were later successfully used to construct the theory of magnetoplastic effects in dislocation crystals with paramagnetic impurities [8]. The question of whether the presence of such impurities is necessary for the sensitivity of diamagnetic crystals to magnetic actions is still open.

In this study, we investigate the effect of a pulsed magnetic field on low-dislocation undoped III–V semiconductor crystals. We found that short-term (seconds) actions of PMFs induced long-term (hundreds of hours) processes of redistribution between components in these compounds. These processes include the formation of clusters of the Group-III-metal component and their following dissolution with an increase in the homogeneity of the crystals. In this case, the presence of paramagnetic impurities is not necessary for the sensitivity of diamagnetic crystals to external magnetic fields. In this study, the effect is discussed for an InAs crystal as a model object.

We used Czochralski indium arsenide single crystals with a carrier concentration of 10^{16} cm^{-3} and examined samples where the dislocation concentration, which was determined from the number of etch pits, did not exceed $\sim 10^3$ cm^{-2}. The samples were cut from the central section of an ingot, and the surface under investigation was mechanically and chemically polished.

The distribution of indium and arsenic over the sample surface was investigated by X-ray spectral microanalysis with a CamScan S4 scanning electron microscope equipped with a Link AN 10/55S system for X-ray energy-dispersion analysis. In the ~1-μm-thick surface layer, the planar distribution of elements was determined from characteristic X-ray radiation induced by an electron beam scanning the surface. X-ray microanalysis was supplemented with differential thermal analysis of samples that were cut from the same crystal and subjected to the same treatment by a pulsed magnetic field.

The action of a pulsed magnetic field was realized by a series of 1500 symmetric triangular 4×10^{-5}-s-long pulses, which had amplitude B = 0.3 T and repeated with frequency f = 50 Hz. Magnetic-field pulses were formed by discharges of a capacitor bank through a low-inductive solenoid. The test samples, along with the control samples that were not subjected to the PMF, were treated and stored at room temperature.

According to X-ray microanalysis, the pulsed magnetic field induces a long-term two-stage process of structural conversions in an InAs crystal. The effect is clearly illustrated in Fig. 1. At the first stage, the crystal surface is enriched in indium that segregates into separate clusters. At the second stage, the precipitating phase is dissolved. Table 1 presents the contents of In and As in various components at different stages of the process. The characteristics of a control sample, which was cut from the same ingot but was not subjected to the PMF, did not vary in this time.

Comparison between the initial and final states of the crystal indicates that PMF action increases the homogeneity of crystal phase composition, at least in the ~1-μm-thick surface layer.

Data of differential thermal analysis, which are presented in Table 2, show that the short-term treatment of the InAs crystal by the PMF noticeably decreases crystal melting temperature T_m.

Comparison between Tables 1 and 2 indicates that the melting temperature of the InAs sample decreases at the stage of the appearance of indium clusters, and the following recovery of sample homogeneity is accompanied by a return of T_m to the initial value.

Voronezh State University,
Universitetskaya pl. 1, Voronezh, 394006 Russia
** e-mail: levin@lev.vsu.ru*

1028-3358/03/4802-0062$24.00

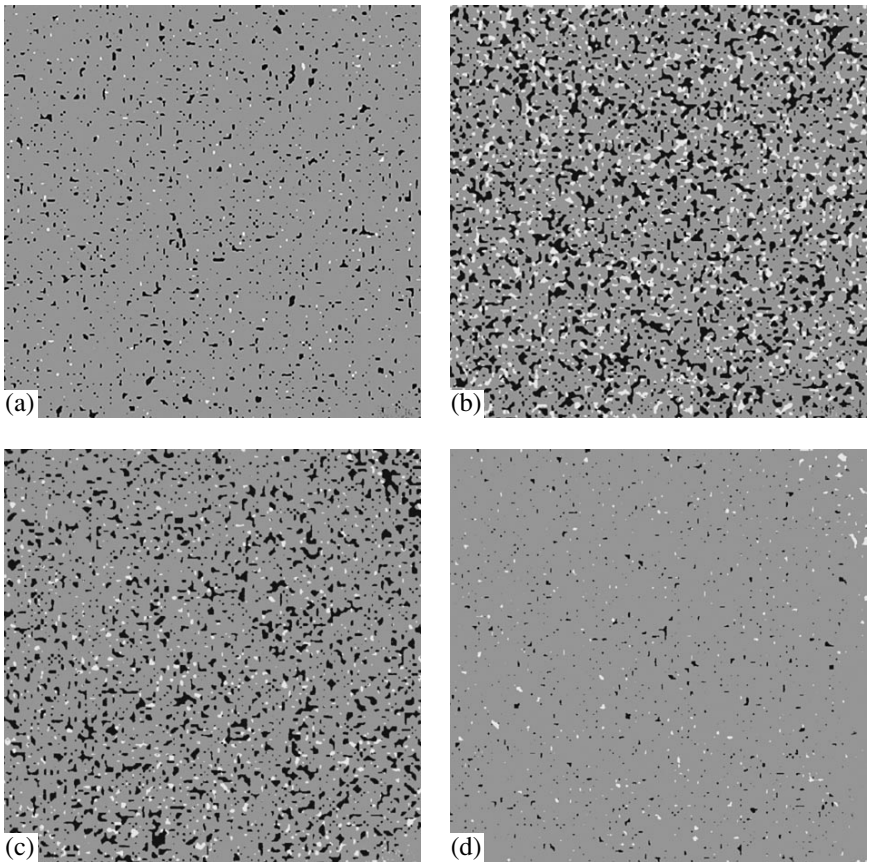

Fig. 1. Phase composition of the ~1-μm-thick surface layer of an InAs crystal (according to X-ray microanalysis): (a) before PMF action and after (b) 5, (c) 10, and (d) 100 d since PMF action. The color of the In, As, and InAs phases is black, white, and gray, respectively.

Any crystal inevitably contains intrinsic associative point defects, whose complexes can have a magnetic moment in the diamagnetic crystal. In particular, the associates of vacancies in semiconductor crystals [9] are among such complexes. If external magnetic fields acting on these complexes induce intercombination transitions, which weaken bonds and lead to the decomposition of the complexes, the defect structure of the crystal will relax, and the structure-sensitive parameters of the crystal will change.

Thus, InAs crystals are sensitive to PMFs due primarily to the presence of complexes that consist of intrinsic point defects and can be decomposed by a weak magnetic field. The nonstoichiometric defects that are associated with vacancies and interstitial Group-V atoms, as well as antisite defects, dominate in III–V compounds [10]. Deviation from stoichiometry in the initial sample was characterized by indium excess. Thus, the principal defects of this sample are associated with an excess content of arsenic vacancies that can form complexes with antisite As_{In} defects [10, 11]. The most probable starting mechanism of the PMF effect on indium arsenide crystals seems to be the weakening of stressed chemical bonds in such vacancy defect complexes due to the PMF-induced intercombination transitions of electrons involved in the formation of these bonds. This process is accompanied by the appearance

Table 1. Relative content of components in the surface layer of an InAs crystal

Component	Before PMF action	After PMF action			
		5 d	10 d	50 d	100 d
As	0.4	3.3	1.3	0.7	0.6
In	4.2	21.4	11.8	7.4	1.6
InAs	95.4	75.3	86.9	91.9	97.8
InAs (without PMF action)	95.4	95.4	95.4	95.4	95.4

Table 2. Melting temperature T_m (in K) of an InAs sample

Sample	Before PMF action	After PMF action			
		5 d	10 d	50 d	100 d
Treated	1210 ± 3	1173 ± 3	1198 ± 3	1203 ± 3	1210 ± 3
Control	1210 ± 3	1210 ± 3	1210 ± 3	1210 ± 3	1210 ± 3

of mobile arsenic vacancies tending to the surface, which is the natural sink for defects. As a result, the surface is enriched in indium with the formation of precipitates. The crystal contains many fewer interstitial arsenic atoms and indium vacancies [12]; therefore, the number of arsenic clusters on the surface increases only negligibly. Individual-element clusters that are formed due to the decomposition of initial defect complexes are metastable and further decomposed with the formation of indium arsenide. As a result, the crystal is homogenized and the number of its defects decreases. The above-mentioned decrease in the melting temperature of the sample can be associated with the appearance of metal precipitates. The duration of the observed processes is determined by the diffusion rate of defects formed due to the decomposition of point-defect complexes at room temperature.

Thus, the presence of paramagnetic impurities is not necessary for the sensitivity of diamagnetic crystals to external magnetic fields, whereas short-term PMF actions on InAs crystals and other III–V semiconductor compounds induce long-term changes in their phase, structural, and thermodynamic states. These changes lead to an increase in the homogeneity of their composition and in the structural perfection of the crystals.

REFERENCES

1. G. I. Distler, V. M. Kanevskiĭ, V. V. Moskvin, *et al.*, Dokl. Akad. Nauk **268** (3), 591 (1983) [Sov. Phys. Dokl. **28**, 43 (1983)].
2. V. N. Davydov, V. A. Loskutova, and E. P. Naĭden, Fiz. Tekh. Poluprovodn. (Leningrad) **23** (9), 1596 (1989) [Sov. Phys. Semicond. **23**, 989 (1989)].
3. V. P. Vlasov, F. A. Zaitov, V. M. Kanevskiĭ, *et al.*, Fiz. Tverd. Tela (Leningrad) **34** (10), 3262 (1992).
4. M. N. Levin and B. A. Zon, Zh. Éksp. Teor. Fiz. **111** (4), 1373 (1997) [JETP **84**, 760 (1997)].
5. V. I. Al'shits, N. N. Bekkauer, A. E. Smirnov, and A. A. Urusovskaya, Zh. Éksp. Teor. Fiz. **115** (3), 951 (1999) [JETP **88**, 523 (1999)].
6. U. E. Steiner and T. Ulrisch, Chem. Rev. **89**, 51 (1989).
7. Ya. B. Zel'dovich, A. L. Buchachenko, and E. L. Frankevich, Usp. Fiz. Nauk **155** (1), 3 (1988) [Sov. Phys. Usp. **31**, 385 (1988)].
8. M. Molotskiĭ and V. Fleurov, Phys. Rev. B **52** (22), 15829 (1995).
9. J. Bourgein and M. Lannoo, *Point Defects in Semiconductors, Experimental Aspects* (Springer, New York, 1983; Mir, Moscow, 1985).
10. M. G. Mil'vidskiĭ and V. B. Osvenskiĭ, *Structural Defects in Semiconductor Single Crystals* (Metallurgiya, Moscow, 1984).
11. S. V. Bulyarskiĭ and V. I. Fistul', *Thermodynamics and Kinetics of Interacted Defects in Semiconductors* (Nauka, Moscow, 1997).
12. G. V. Semenova, T. P. Sushkova, and E. G. Goncharov, Zh. Neorg. Khim. **39** (10), 1612 (1994).

Translated by V. Bukhanov

Doklady Physics, Vol. 48, No. 2, 2003, pp. 65–69. Translated from Doklady Akademii Nauk, Vol. 388, No. 6, 2003, pp. 751–756.

PHYSICS

Destruction of the Phase Transition to the Crystalline State in a Strong Electric Field

S. V. Shevkunov

Presented by Academician V.V. Osiko October 14, 2002

Received October 4, 2002

In this study, the mechanism of the destruction of the crystallization phase transition in systems of polar particles is analyzed. In electric fields exceeding the critical value, the interface between the crystalline and liquid phases disappears, and the system transits to a specific superpolarized state. This transition is accompanied by a qualitative change in interparticle correlations. Transformation to the superpolarized state is a first-order phase transition with heat absorption. In view of the problem of chlorine accumulation in the polar stratosphere, Monte Carlo simulation of water-molecule clusters is carried out on a computer. The electric field of ions near the surface of ice single crystals can induce local destruction of the microrelief fragments immediately before the implantation of ions under the surface. This mechanism is responsible for the strong dependence of adsorptivity of the ice surface on the method of its preparation.

1. INTRODUCTION

The theory of phase transitions is one of the complex items of equilibrium statistical mechanics. According to Yang–Lee theory [1, 2], sharp changes in the equilibrium properties of a substance are attributed to the zeros of the analytic continuation of the large partition function to the complex plane of the chemical potential. The zeros of the partition function correspond to the singularities of the free energy. The number of zeros is equal to the number of particles in the system, and there are no real zeros. As the number of particles increases, zeros reproduce and are grouped to lines. In the thermodynamic limit $N \longrightarrow \infty$, the first derivative of the free energy can have a discontinuity at the intersection point of such a line with the real axis. This discontinuity is classified as a first-order phase transition. There is no universal dependence between the number of phase transitions in the system and the nature of its constituent particles. Theoretical predictions of the position of coexistence curves in the phase diagram require enormous computer calculations in each particular case.

Strictly speaking, phase transitions as the singularities of corresponding thermodynamic functions are impossible in systems containing a limited number of particles. However, the closeness of singularities to the real axis of the chemical potential is manifested as smoothed, but sufficiently sharp, changes in the behavior of the free energy and its derivatives. During the last three decades, the minimum number of particles for which phase states and transitions between them become distinguishable was estimated by computer simulation. In contrast to initial expectations, the collective behavior is manifested even in extremely small ensembles. The traces of phase transitions are observed in systems consisting of only a few tens of molecules and even several molecules, but the transition points in small systems are usually shifted to low temperatures.

Ice microcrystals are attracting increased interest. Comprehensive computer simulations [3–6] showed that the melting temperatures of clusters consisting of ten to several tens of water molecules lie in the range from 150 to 220 K, which corresponds to the polar stratosphere. Small water clusters are in the quasiliquid state at stratosphere temperatures. The elements of a microrelief on the surfaces of ice crystals are molecular clusters and can be in solid or melted states depending on their sizes. Under natural temperature variations, small irregularities are melted first. The phase state of the ice surface under the conditions of the polar stratosphere is of interest in view of the problem of the destruction of the protective ozone layer in the upper atmosphere. Ozone is destroyed in the reaction of chlorine oxidation. In turn, chlorine in the form of compounds that are chemically inactive with respect to ozone, such as HCl, is accumulated in ice microcrystals appearing in specific clouds in the stratosphere [7, 8]. The high adsorptivity of the ice surface with respect to HCl is the key property responsible for the multiple repetition of the destroying cycle. The large spread of the ice adsorptivity values measured in various laboratory experiments [9, 10] testifies to the strong dependence of the adsorption mechanism on the relief and

St. Petersburg State Technical University,
ul. Politekhnicheskaya 29, St. Petersburg, 195251 Russia
e-mail: root@shevk.hop.stu.neva.ru

1028-3358/03/4802-0065$24.00

phase state of the surface. Computer simulation [11] shows that the mechanism of simple physisorption without the preliminary dissociation of a HCl molecule into ions cannot provide the high ice-adsorptivity values measured in experiments. A stable hydrate shell is formed in the field of singly charged ions under the natural conditions of the moist atmosphere [12]. Intermolecular correlations in the hydrate shell are similar to those in a liquid over a wide temperature range. Transition to the crystalline state is not observed.

Ions are sources of a strong electric field. The field reaches a value of 3×10^7 V/cm between two singly charged opposite ions at a distance of 20 Å. This field is comparable with local molecular fields and can therefore considerably affect the stability of the phase state. The electric field of a chlorine ion can change the phase state of the microrelief elements on the ice surface at the point where the ion penetrates and, as a result, affect the adsorptivity of the microrelief. An external electric field can provide both consolidating and destructive effects on the ordered phase. This study aims to examine the effect of an external electric field on the melting of water molecular clusters.

2. TECHNIQUE

Computer simulation of ice clusters is carried out by the Monte Carlo method in the canonical statistical ensemble [13]. Canonical averages are calculated by directly averaging over molecular configurations according to the Gibbs equilibrium distribution functions. The application of the methods of computer simulation near the points of phase transitions requires the accumulation of large statistics. The description of melting is particularly difficult due to the relatively low mobility of particles. In order to obtain reliable data, Markov processes are generated with a length of (8–800) $\times 10^6$ steps, which are one to two orders larger than the accepted standards. The procedure of slow variation in external conditions is used; i.e., the last configuration of the preceding Markov chain is used as an initial configuration for the next chain. The first 10% of steps are not used in calculation of averages. The typical values of maximum displacement and turn of molecules per step are 0.2 Å and 12°, respectively. About 50% of new configurations are accepted.

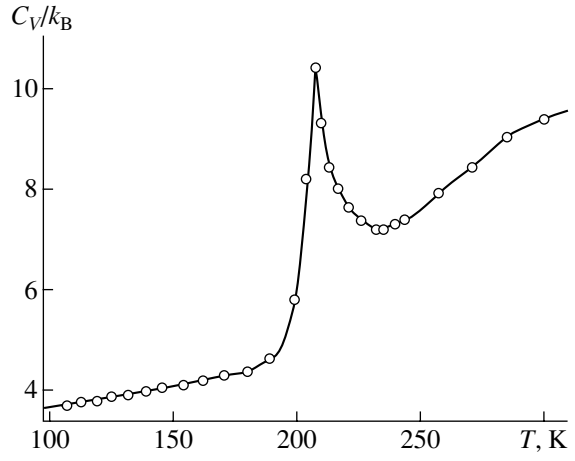

Fig. 1. Heat capacity per molecule (without the kinetic part $3k_B$) in a $(H_2O)_{40}$ cluster.

Interactions between molecules are described by the Rahman–Stillinger ST2 potential [14, 15]. The system is exposed to an external electric field of $E = (0.7–7) \times 10^7$ V/cm. The energy of interaction with the external field consists of the Coulomb energy of point charges entering into the ST2 potential and the polarization energy of molecules $u_{\text{pol}}^{w-\text{field}} = -\alpha_w \frac{E^2}{2}$, where $\alpha_w = 1.44$ Å^3 is the isotropic polarizability of the water molecule. To prevent the evaporation of a cluster to vacuum, the system is placed into a spherical cavity of radius $R_0 = 12$ Å. To prevent the direct contact of the cluster with the wall, one of cluster molecules is fixed at the center of the cavity. The heat capacity

$$C_v = \frac{\langle U^2 \rangle - \langle U \rangle^2}{k_B T}$$

and polarizability tensor

$$\alpha_{\alpha\beta} = \frac{\langle P_\alpha P_\beta \rangle - \langle P_\alpha \rangle \langle P_\beta \rangle}{k_B T} + \delta_{\alpha\beta} N \alpha_w,$$

as well as the inner energy $\langle U \rangle$ and mean dipole moment $\langle \mathbf{P} \rangle$, are calculated by the fluctuation theorem. The cluster structure is analyzed by means of atom–atom and angular intermolecular correlation functions.

3. RESULTS OF SIMULATION

3.1. Melting

The transition of a $(H_2O)_{40}$ cluster to the crystalline state at temperature $T_{\text{melt}} = 208$ K is identified due to the sharp change in the slope of the temperature dependence of the internal energy $\langle U \rangle$. The slope per molecule changes stepwise from $10k_B$ to $4k_B$. The latter value differs from the heat capacity $3k_B$ of the harmonic oscillator with six degrees of freedom by 30%, which can be accepted as the estimate of the anharmonicity of the system in the state close to melting. The heat capacity calculated from energy fluctuations has a strong maximum at the transition point (Fig. 1). The curve of electric polarizability is approximately similar. For comparison, melting of the $(H_2O)_6$ and $(H_2O)_8$ clusters was observed at 50 and 160 K, respectively [3].

It is important to find structural characteristics that can serve as reliable indicators of cluster melting. We comprehensively studied the behavior of the $g_{OO}(R)$, $g_{OH}(R)$, and $g_{HH}(R)$ atom–atom correlation functions at melting and found no fundamental changes in their form at the transition point. The melting in water clus-

ters is accompanied by finer structural changes than those detectable by means of these functions. In a macroscopic system, melting is accompanied by the destruction of the far molecular order. The far order is absent in clusters due to their microscopic sizes. However, sharp changes in the internal energy and heat capacity of clusters indicate that the absence of far order does not mean the complete disappearance of the traces of a phase transition. The change in the short order is responsible for the sharp increase in energy fluctuations at the point of the phase transition. Our investigations show that melting in water clusters is accompanied by a sharp change in correlation between the molecular positional and orientational orders. The orientational order is not destroyed completely at melting, but the prevailing orientation of molecules becomes slightly dependent on the intermolecular distance, and this dependence is modified from oscillatory to monotonic (see Fig. 2). The correlations of distances between molecules and their relative orientations weaken at melting. These correlations are binary, but additional resolution of the angle is performed in the function shown in Fig. 2, in contrast to the correlations represented by the $g_{OO}(R)$, $g_{OH}(R)$, and $g_{HH}(R)$ functions. The initial binary correlation function of molecules depends on 6 + 6 = 12 spatial variables. Both types of correlation functions are formally obtained by folding in various sections of the hypersurface corresponding to the initial correlation function. The most substantial changes at melting occur in the subspace involving angular variables. Thus, the change in correlation between the spatial positions of molecules and their mutual orientations is the essence of structural changes occurring in water clusters at melting. Although melting in a macroscopic phase is commonly associated with the destruction of the far molecular order, changes in the short order can likely significantly contribute to sharp changes in the caloric state of the system. This conclusion is supported by the pronounced maxima in heat capacity at the transition point in clusters (see Fig. 2) where far order is impossible in principle.

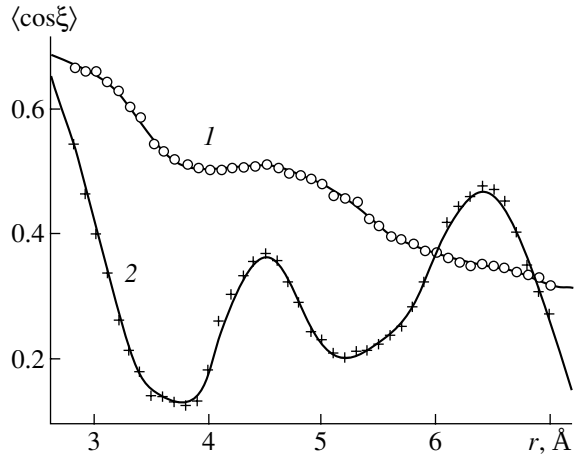

Fig. 2. Binary angular intermolecular correlation functions in a $(H_2O)_{40}$ cluster, i.e., the mean cosine of the angle between the dipole moment of the second water molecule and vector **r** joining the oxygen atoms of the first and second molecules, for (*1*) 244 and (*2*) 199 K.

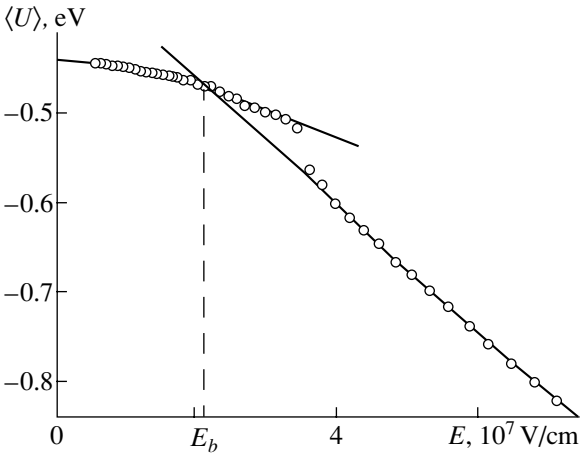

Fig. 3. Mean energy of intermolecular interactions in a $(H_2O)_{40}$ cluster per molecule vs. the external electric field at 150 K.

3.2. Effect of an External Electric Field

The dependence of the cluster internal energy U on the applied electrostatic field is obtained at a constant temperature of 150 K and is shown in Fig. 3. Two branches separated by a jump are observed. The change in the curve slope when passing from one branch to another implies a sharp change in the induced dipole moment of the cluster. Independent calculation shows that the dipole moment changes by a factor of 2–3. The longitudinal component of the cluster polarizability tensor has a pronounced maximum at the boundary between two branches, while this maximum is absent in the transverse component. In the external field, the electric properties of the cluster are strongly anisotropic. The longitudinal polarizability of the cluster is less than the transverse polarizability by a factor of 2–3 everywhere except the narrow region near the maximum. Similar dependences were obtained for temperatures of (crystalline state) 170, 200, and (liquid state) 240 K.

At temperatures of 150, 170, and 200 K, as the weak field becomes strong, the angular correlation functions such as those shown in Fig. 2 change qualitatively from oscillating to monotonic; i.e., the crystalline order is stepwise destroyed, and a strongly polarized state is formed. In this state, the dipole moments of molecules are almost parallel to the field lines of the external field, and the dipole moment of the cluster differs from its theoretical limit only by 5–10%. As the field increases, the structure of the cluster in both crystalline and liquid states changes to a new thermodynamically stable state, which is referred to as the superpolarized state. This

superpolarized state is characterized by the destruction of strong intermolecular correlations inherent in the condensed phase and by the formation of the monotonic orientational molecular order induced by the external field. The transition itself in the strong field is not surprising, but its stepwise behavior is nontrivial. As the cluster size increases, the transition becomes sharper. It is reasonable to think that the transition becomes a phase transition in the strict sense at the macroscopic limit.

The type of the phase transition depends on its latent heat $N\lambda$. Competition between two possible states of the system is determined by the ratio of Gibbs free energies

$$G_n(E, T) = U_n - TS_n + pV_n$$

for a normal (crystalline or liquid) state and

$$G_s(E, T) = U_s - TS_s + pV_s$$

for a superpolarized state. At the transition point,

$$G_n(E, T) = G_s(E, T).$$

Neglecting small effects associated with the difference of volumes V_n and V_s, we obtain the following expression for the jump of the internal energy at the transition point:

$$\Delta U = U_S - U_N = T(S_s - S_n) = N\lambda. \quad (1)$$

This expression determines the sign of λ and which of two the phases is more ordered (has lower entropy S). At first glance, since ΔU is negative in Fig. 3, λ is also negative, and the superpolarized state is more ordered. However, this conclusion is inconsistent with the temperature dependence of the position of the transition point. Comparison of the dependences obtained for 150, 170, 200, and 240 K shows that, as temperature increases, the transition to the superpolarized state occurs at weaker fields; i.e., $\frac{dE_{tr}}{dT_{tr}} < 0$, which inevitably leads to the positive sign of λ. Indeed, the chemical potentials of the phases at their interface in the E–T diagram are equal to each other. Therefore, the same is true for their differentials along the phase interface:

$$d\mu_n = -\frac{P_n}{N}dE_{tr} - \frac{S_n}{N}dT_{tr} + \frac{V_n}{N}dp_{tr},$$

$$d\mu_s = -\frac{P_s}{N}dE_{tr} - \frac{S_s}{N}dT_{tr} + \frac{V_s}{N}dp_{tr},$$

where P_n and P_s are dipole moments of the system in two states. When pressure p is constant, we arrive at the following analogue of the Clapeyron–Clausius equation for the system in the electric field:

$$\frac{dE_{tr}}{dT_{tr}} = -\frac{S_s - S_n}{P_s - P_n} = -\frac{\lambda}{T_{tr}(P_s - P_n)}, \quad (2)$$

from which it follows that $\lambda > 0$ and $\Delta U > 0$.

To reveal the causes of the discrepancy between the positive sign following from Eq. (2) and the negative sign of ΔU in Fig. 3, we repeat calculation of the curve in Fig. 3 in the opposite direction, i.e., from strong to weak fields. The calculation shows the presence of a strong hysteresis near the structural transition, which in turn testifies to the metastable state. This behavior of the system near the structural transition is natural and is almost always observed near the melting point when simulating systems with sufficiently complex intermolecular interaction. In this case, the time of the establishment of thermodynamic equilibrium increases sharply, and we deal with states that are close to equilibrium states but do not coincide with them. In Fig. 3, the points in the curve between 2.1×10^7 and 3.5×10^7 V/m correspond to metastable states (overheated normal phase).

In opposite-direction calculations, the points of structural transitions are shifted towards weaker fields. However, $\frac{dE_{tr}}{dT_{tr}}$ is negative. Therefore, the positive sign of λ that is determined from Eq. (2) is beyond question. We determine the real position of the transition point by the following iterative procedure. We set $\lambda = 0$, i.e., $\Delta U = 0$, in the first approximation and extrapolate the branch corresponding to the superpolarized state to the region of the normal state (see Fig. 3). The intersection point E_b would correspond to the second-order phase transition without change in entropy. However, the observed temperature dependence of the transition point implies that $\lambda \neq 0$. The value of the right-hand side of Eq. (2) is determined from curves $U(E)$ for various temperatures. The resulting λ value, together with $\Delta U \neq 0$, obtained from Eq. (2) is used to determine the point of the phase transition in the next iteration, etc. The transition points calculated in such a way are shifted to weak fields by 20–30% with respect to the points where the jump of the internal energy is obtained in the Monte Carlo simulation, and the shift is larger for low temperatures.

Figure 4 shows the approximate scheme of the position of interfaces between different thermodynamic states of the cluster according to the results obtained above. In the region of the normal state in a relatively weak electric field, an increase in the field shifts the melting point to low temperatures; i.e., the external field facilitates the melting of clusters. In sufficiently strong fields (in the region of the superpolarized state in Fig. 4), the difference between the crystalline and liquid states of the system disappears. A strong electric

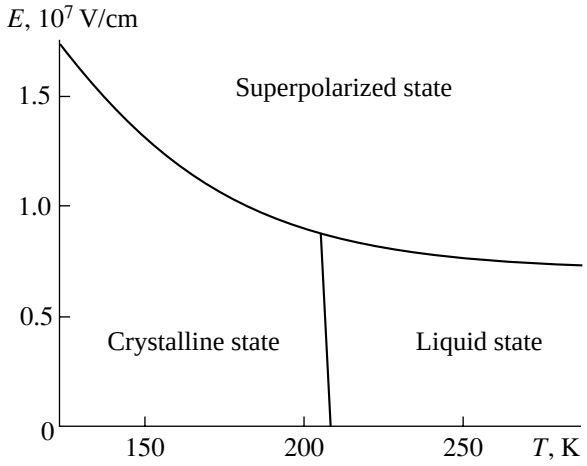

Fig. 4. Schematic *E–T* diagram of various states of a $(H_2O)_{40}$ cluster according to computer simulation.

field destroys the melting phase transition, and this destruction is stepwise.

4. CONCLUSIONS

The results are summarized as follows. The structural transition from the liquid to crystalline state is clearly observed in a cluster consisting of 40 water molecules. This transition is accompanied by sharp changes in the thermodynamic characteristics and is characterized by a maximum in the heat capacity. Melting is primarily manifested in the short orientational molecular order: correlations between the mutual orientation and distances between molecules weaken sharply. A weak electric field decreases the melting temperature of the cluster. A strong field destroys the melting phase transition altogether. The transition from the weak-field mode to the strong-field mode is a first-order phase transition. In the strong electric field, a specific, thermodynamically stable, superpolarized state is formed, where strong intermolecular correlations inherent in the condensed phase are destroyed. Despite the prevailing orientation of molecules along the field, the superpolarized state is less ordered compared to both the liquid and crystalline states. This state has higher entropy, because the positions of molecules fluctuate more strongly due to the destruction of the network of hydrogen bonds between molecules. The transition to the superpolarized state is accompanied by heat absorption.

ACKNOWLEDGMENTS

This work was supported by INTAS (grant no. 99-01162).

REFERENCES

1. T. L. Hill, *Statistical Mechanics. Principles and Selected Applications* (McGraw-Hill, New York, 1956).
2. L. D. Landau and E. M. Lifshitz, *Course of Theoretical Physics*, Vol. 5: *Statistical Physics* (Nauka, Moscow, 1995; Pergamon, Oxford, 1980).
3. J. Rodriguez, D. Laria, E. J. Marceca, and D. A. Estrin, J. Chem. Phys. **110**, 9039 (1999).
4. P. Nigra, M. A. Carignano, and S. Kais, J. Chem. Phys. **115**, 2621 (2001).
5. S. V. Shevkunov, Dokl. Akad. Nauk **376**, 318 (2001) [Dokl. Phys. **46**, 12 (2001)].
6. A. Vegiri and S. V. Shevkunov, J. Chem. Phys. **115**, 4175 (2001).
7. J. C. Farman, B. G. Gardiner, and J. D. Shanklin, Nature (London) **315**, 207 (1985).
8. S. M. Solomon, R. R. Garcia, F. S. Rowland, and D. J. Wuebbles, Nature (London) **321**, 755 (1986).
9. H. A. Donsig and J. C. Vickerman, Faraday Discuss. **100**, 348 (1995).
10. M.-T. Leu, L. F. Keyser, and R. S. Timonen, J. Phys. Chem. B **101**, 6259 (1997).
11. G. J. Kroes and D. C. Clary, J. Phys. Chem. **96**, 7079 (1992).
12. S. V. Shevkunov, Zh. Éksp. Teor. Fiz. **105**, 1258 (1994) [JETP **78**, 677 (1994)].
13. V. M. Zamalin, G. E. Norman, and V. S. Filinov, *The Monte-Karlo Method in Statistical Thermodynamics* (Nauka, Moscow, 1977).
14. A. Rahman and F. H. Stillinger, J. Chem. Phys. **55**, 3336 (1971).
15. F. H. Stilliger and A. Rahman, J. Chem. Phys. **57**, 1281 (1972).

Translated by R. Tyapaev

Doklady Physics, Vol. 48, No. 2, 2003, pp. 70–74. Translated from Doklady Akademii Nauk, Vol. 388, No. 4, 2003, pp. 472–476.

TECHNICAL PHYSICS

New Method of Approximating the Field-Amplitude Distribution in an Antenna Aperture by Atomic Functions

V. F. Kravchenko

Presented by Academician Yu.V. Gulyaev September 24, 2002

Received September 24, 2002

In this study, we investigated the spectral properties of the family of atomic functions (AFs) [1–4] in connection with the aperture theory of antennas [5–7]. Several basic cases are considered: AFs and the family of cosine, truncated Gaussian, and Taylor even amplitude distributions in an antenna aperture. The method is based on the constructive theory of AFs described in [2–4].

FUNDAMENTAL RELATIONSHIPS BETWEEN THE PHYSICAL PARAMETERS OF AN ANTENNA

The physical parameters of large antennas are described by the following relationships [5, 6].

1. Directivity-diagram maximum

$$F_m \equiv F(0) = \omega \int_{-1/2}^{1/2} g(x')dx'. \quad (1)$$

Here, x is the coordinate in the aperture plane, ω is the full width along this coordinate, and the prime denotes a normalized dimensionless variable, for example, $x' = \frac{x}{\omega}$ and $u' = u\omega = \frac{\omega}{\lambda}\sin\theta\cos\varphi$.

2. Total radiated power

$$P_{\text{rad}} \equiv \int_{-\infty}^{\infty} |F(u)|^2 du = \int_{-\omega/2}^{\omega/2} |g(x)|^2 dx = \omega \int_{-1/2}^{1/2} |g(x')|^2 dx'. \quad (2)$$

3. Aperture efficiency factor

$$\eta_x = \frac{|F_m|^2}{\int_{-\infty}^{\infty} |F(u')|^2 du'} = \frac{\left|\int_{-1/2}^{1/2} g(x')dx'\right|^2}{\int_{-1/2}^{1/2} |g(x')|^2 dx'}. \quad (3)$$

4. Noise beam width (in radians)

$$\omega_{\text{n}} = \frac{\omega \int_{-1/2}^{1/2} |g(x')|^2 dx'}{|g_m(x')|^2}. \quad (4)$$

5. Noise aperture width (in x-coordinate units)

$$\omega_{\text{n}} = \frac{\omega \int_{-1/2}^{1/2} |g(x')|^2 dx'}{|g_m(x')|^2}. \quad (5)$$

6. Root-mean-square aperture width (according to radiation power, in x-coordinate units)

$$L_{\text{s}} = 2\pi\omega \left[\frac{\int_{-1/2}^{1/2} x'^2 |g(x')|^2 dx'}{\int_{-1/2}^{1/2} |g(x')|^2 dx'}\right]^{1/2}. \quad (6)$$

7. Root-mean-square beam width (in radians)

$$\theta = \frac{\lambda}{\omega}\left[\frac{\int_{-1/2}^{1/2} \left|\frac{dg(x')}{dx'}\right|^2 dx'}{\int_{-1/2}^{1/2} |g(x')|^2 dx'}\right]^{1/2}. \quad (7)$$

Institute of Radio Engineering and Electronics, Russian Academy of Sciences, ul. Mokhovaya 18, Moscow, 103907 Russia

1028-3358/03/4802-0070$24.00

Table 1. Parameters of new Kravchenko weighting functions (antenna windows) and of cosine field distributions in aperture

No.	Type of weighting-function distribution	F_m	SLL, dB	Band at 6-dB level, rad	P_{rad}	η_x	$J(w)$
1	Kravchenko ($\text{fup}_2(x)$)	0.6537	–27.3	0.7250	0.4980	0.8580	1.9428
2	Kravchenko ($\Xi_2(x)$)	0.6923	–34.1	1.1750	0.5299	0.9046	1.3157
3	Kravchenko ($\Xi_3(x)$)	0.6475	–45.7	1.3250	0.4929	0.8508	1.0088
4	$\cos(\pi x)$	0.6366	–23.2	0.7750	0.5000	0.8106	2.3128
5	$\cos^2(\pi x)$	0.5000	–32.0	0.9250	0.3750	0.6667	2.0583
6	$\cos^3(\pi x)$	0.4244	–40.0	1.0750	0.3125	0.5764	1.6867
7	$\cos^4(\pi x)$	0.3750	–46.7	1.2250	0.2734	0.5143	1.8373
8	$\cos^5(\pi x)$	0.3395	–53.9	1.3250	0.2461	0.4684	1.9460
9	$\cos^6(\pi x)$	0.3125	–61.0	1.4750	0.2256	0.4329	2.0290

8. Ratio of voltage-curve slope at the beam center to slope for a linear odd amplitude distribution

$$K_{\text{r}} = \sqrt{12}\frac{\int_{-1/2}^{1/2} x'g(x')dx'}{\left[\int_{-1/2}^{1/2} |g(x')|^2 dx'\right]^{1/2}}. \quad (8)$$

9. Quality functional of new weighting functions. To find the optimal weighting functions (antenna windows), we construct the quality functional

$$J(w) = \|w - w_{\text{st}}\|_{l_4^2[-1;\,1]} = \min. \quad (9)$$

The construction procedure involves several stages. At the first stage, we determine the necessary physical parameters of the weighting functions (antenna windows) according to Eqs. (1)–(7); at the second stage, we find the quality functional $J(w)$ for particular distributions. The quality functional is written in the following form (it represents the norm in the space of distribution parameters, and we take only four parameters):

$$\begin{aligned} J(w) &= J(F_m(w), l_{\text{st}}(w), P_{\text{rad}}(w), \eta_x(w)) \\ &= A_1\left(\frac{F_m(w_i) - F_m(w_{\text{st}})}{F_m(w_{\text{st}})}\right)^2 \\ &+ A_2\left(\frac{l_{\text{sl}}(w_i) - l_{\text{sl}}(w_{\text{st}})}{l_{\text{sl}}(w_{\text{st}})}\right)^2 \\ &+ A_3\left(\frac{P_{\text{rad}}(w_i) - P_{\text{rad}}(w_{\text{st}})}{P_{\text{rad}}(w_{\text{st}})}\right)^2 \\ &+ A_4\left(\frac{\eta_x(w_i) - \eta_x(w_{\text{st}})}{\eta_x(w_{\text{st}})}\right)^2. \end{aligned} \quad (10)$$

Here, w_{st} is the standard distribution with the parameters $F_m = 1$, $l_{\text{sl}} = -45$ dB, $P_{\text{rad}} = 1$, $\eta_x = 1$; $A_1 = A_3 = A_4 = 1$ and $A_2 = 3$ are the weighting coefficients. The minimum values of the functional correspond to optimal windows.

ATOMIC FUNCTIONS AND THE FAMILY OF COSINE FIELD DISTRIBUTIONS

We consider the family of cosine amplitude distributions. Its basic parameters and distributions calculated by Eqs. (1)–(10) are presented in Table 1. The quality functional $J(w)$ in this table indicates that most distributions have better basic physical characteristics than the family of cosine distributions.

ATOMIC FUNCTIONS AND THE GAUSSIAN TRUNCATED FIELD-AMPLITUDE DISTRIBUTIONS

Such a distribution is of interest, because its Fourier transform also gives the Gaussian curve. This fact enables us to make a number of certain generalizations. In this case, it is necessary to provide a field decrease at the aperture edge almost to zero, i.e., by more than 20 dB. In this case, the limits of integration extend to infinity according to the requirements of the Fourier transform, and the integral becomes the Gauss second integral. Thus, the constructed directivity diagram has no side lobes but is not used in practice due to its small effective aperture area. In our case, the truncated Gaussian amplitude distributions are constructed according to the relationship

$$G(n, x) = \exp(-1.382(nx)^2).$$

Analysis of quality functional (10) shows that most of our amplitude distributions have better physical characteristics than the Gaussian distribution. Table 2 presents certain new amplitude distributions (antenna windows) [in descending order of the side-lobe level (SLL)] for comparison with the Gaussian distribution. As the numerical experiment shows, all these distribu-

Table 2. Parameters of new Kravchenko weighting functions and of the Gaussian truncated field distribution in an aperture

No.	Type of weighting-function distribution	F_m	SLL, dB	Band at 6-dB level, rad	P_{rad}	η_x	$J(w)$
1	Kravchenko ($\text{fup}_{30}(x)$)	0.9399	–14.4	0.5750	0.8869	0.9960	2.0972
2	Kravchenko ($\text{fup}_4(x)$)	0.7414	–20.9	0.6750	0.5925	0.9277	2.1709
3	Kravchenko–Bernstein ($\text{fup}_2(x) \cdot \text{Br}(x)$)	0.4974	–38.4	0.9250	0.3676	0.6730	1.5820
4	Kravchenko–Bessel ($\text{fup}_4^2(x) \cdot J_0^4(x)$)	0.4992	–43.7	0.8750	0.3589	0.6944	1.4475
5	Kravchenko ($\Xi_4(x)$)	0.5929	–58.0	1.4750	0.4386	0.8016	1.1669
6	Kravchenko ($\Xi_5(x)$)	0.5528	–70.5	1.6250	0.4041	0.7564	1.2867
7	Kravchenko ($\Xi_6(x)$)	0.5182	–83.2	1.7250	0.3752	0.7157	1.3909
8	Gauss ($G(1; x)$)	0.8951	–15.5	0.5750	0.8100	0.9892	2.1432
9	Gauss ($G(1.7; x)$)	0.7467	–20.7	0.6750	0.5984	0.9319	2.1705
10	Gauss ($G(2.4; x)$)	0.5992	–36.6	0.7750	0.4421	0.8121	1.4016
11	Gauss ($G(2.8; x)$)	0.5277	–36.7	0.8750	0.3804	0.7320	1.6074
12	Gauss ($G(3.2; x)$)	0.4675	–46.7	0.9750	0.3331	0.6560	1.5434

Table 3. Parameters of new Kravchenko weighting functions and of Taylor even field-amplitude distributions in an aperture

No.	Type of weighting-function distribution	F_m	SLL, dB	Band at 6-dB level, rad	P_{rad}	η_x	$J(w)$
1	Kravchenko ($\text{fup}_{50}(x)$)	0.9619	–13.9	0.5750	0.9272	0.9978	2.0706
2	Kravchenko ($\text{fup}_{45}(x)$)	0.9581	–14.0	0.5750	0.9201	0.9976	2.0742
3	Kravchenko ($\text{fup}_{40}(x)$)	0.9534	–14.1	0.5750	0.9115	0.9972	2.0804
4	Kravchenko ($\text{fup}_{35}(x)$)	0.9475	–14.2	0.5750	0.9007	0.9967	2.0901
5	Kravchenko ($\text{fup}_4(x) \cdot \text{br}(x)$)	0.5355	–32.7	0.8750	0.3998	0.7172	1.8950
6	Kravchenko ($\text{fup}_4^2(x) \cdot J_0^4(x)$)	0.5408	–37.2	0.8250	0.3925	0.7452	1.5315
7	Kravchenko ($\text{fup}_2^2(x)$)	0.4980	–42.9	0.9250	0.3610	0.6869	1.4541
8	Taylor ($T_{-20}(x)$)	0.7582	–20.8	0.6250	0.6044	0.9510	2.1264
9	Taylor ($T_{-25}(x)$)	0.6923	–25.6	0.6750	0.5315	0.9016	1.9546
10	Taylor ($T_{-30}(x)$)	0.6416	–30.5	0.7250	0.4827	0.8529	1.7353
11	Taylor ($T_{-35}(x)$)	0.6003	–35.2	0.7750	0.4462	0.8076	1.5059
12	Taylor ($T_{-40}(x)$)	0.5660	–40.3	0.8250	0.4176	0.7672	1.2492
13	Taylor ($T_{-45}(x)$)	0.5367	–45.0	0.8750	0.3939	0.7314	1.3380

tions have higher radiated power compared to the Gaussian distribution for an approximately equal SLL.

ATOMIC FUNCTIONS AND EVEN TAYLOR AMPLITUDE DISTRIBUTIONS

In 1953, T.T. Taylor proposed a new class of aperture distributions extensively used not only in the theory of antennas but also in various fields of modern radiophysics. A detailed derivation of various relationships obtained by Taylor in connection with the problems of the field-amplitude distribution in the aperture was given in [7]. It should be noted that, in contrast to our amplitude distributions (antenna windows) based on AF theory, the Taylor expressions have a heuristic basis; nevertheless, they give good results in engineering calculations. Table 3 shows the parameters of the Taylor amplitude distributions and Kravchenko amplitude distributions (antenna windows). The spectral

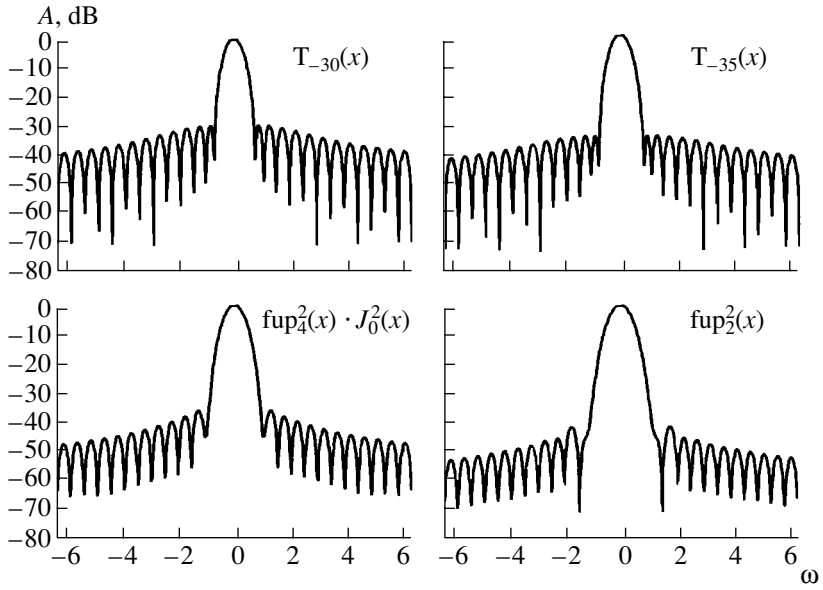

Spectral characteristics of Taylor amplitude distributions $T_{-30}(x)$ and $T_{-35}(x)$ and Kravchenko–Bessel $\text{fup}_4^2(x) \cdot J_0^2(x)$ and Kravchenko $\text{fup}_2^2(x)$ new antenna windows.

characteristics of these distributions are also compared in the figure.

APERTURE FIELD DISTRIBUTION IN TERMS OF ATOMIC FUNCTIONS WITH A LOW SIDE-LOBE LEVEL

The results of numerical experiments with new amplitude distributions (antenna windows) based on AFs [1–4] (see Table 4) illustrate the considerable potential of the method under consideration for solving the problems of antenna engineering. Physical analysis of numerical results for the basic physical parameters indicates that new distributions have a very low SLL and that their quality functional (10) ranges from 1.50 to 1.75. In this case, the SLL is no more than –42 dB. Below, this statement will be illustrated for the problems of analysis and synthesis of antennas. As is known [4, 7–9], current methods of synthesis are divided into two groups depending on the character of a preset

Table 4. Parameters of new Kravchenko weighting functions (antenna windows) with a low side-lobe level

No.	Type of weighting-function distribution	F_m	SLL, dB	Band at 6-dB level, rad	P_{rad}	η_x	$J(w)$
1	Kravchenko–Bernstein $\text{fup}_4(x) \cdot \text{Br}^2(x)$	0.4428	−42.2	1.0250	0.3249	0.6035	1.6288
2	Kravchenko–Bessel $\text{fup}_2^2(x) \cdot J_0(x)$	0.4806	−44.5	0.9250	0.3473	0.6650	1.5071
3	Kravchenko–Bessel $\text{fup}_2^2(x) \cdot J_0^2(x)$	0.4647	−45.9	0.9750	0.3350	0.6447	1.5556
4	Kravchenko–Bernstein $\text{fup}_2(x) \cdot \text{Br}^2(x)$	0.4203	−45.8	1.0750	0.3072	0.5750	1.6975
5	Kravchenko $\text{fup}_4^4(x)$	0.4371	−52.2	1.0250	0.3114	0.6136	1.6379
6	Kravchenko–Bernstein $\text{fup}_4^2(x) \cdot \text{Br}(x)$	0.4661	−54.1	0.9750	0.3398	0.6393	1.5548
7	Kravchenko–Bernstein $\text{fup}_2^2(x) \cdot \text{Br}(x)$	0.4166	−55.1	1.0750	0.3021	0.5743	1.7070
8	Kravchenko–Bessel $\text{fup}_4^4(x) \cdot J_0^2(x)$	0.4131	−57.7	1.0750	0.2937	0.5809	1.7123
9	Kravchenko–Bernstein $\text{fup}_4^2(x) \cdot \text{Br}^2(x)$	0.3998	−64.5	1.1250	0.2898	0.5517	1.7587
10	Kravchenko–Chebyshev $\text{fup}_4(x) \cdot \text{Cheb}_3(x)$	0.4247	−65.5	1.0750	0.3055	0.5904	1.6794

directivity diagram. The first group involves the methods of synthesis of pencil-beam antennas with a low SLL. In this case, the problem of synthesis reduces either to the optimization of the main lobe width and of the SLL or to the achievement of the maximum directivity under certain restrictions on the basic characteristics of the antenna. The Taylor method of synthesis of the antenna with the minimum main-lobe width for a specified SLL was considered in [7]. Other methods of synthesis of pencil-beam antennas and the problems of superdirectivity using AFs will be considered in future. The second group of methods of synthesis is applied to antennas with a special shape of the directivity diagram. Here, the mathematical technique of the theory of functions [5, 7], which was developed by Bakhrakh and Kremenetskiĭ [8] and Zelkin and Sokolov [9], is used. The results (see Table 4) are of certain theoretical and practical interest both for the determination of the field distribution in the aperture and the synthesis of antennas according to the specified directivity diagram and to the superdirectivity phenomenon.

CONCLUSIONS

Thus, we proposed and justified a new method of approximating the field-amplitude distribution in an antenna aperture by atomic functions. The numerical experiment, as well as physical analysis of the results and their comparison with known classical data, corroborated the efficiency and reliability of this method, which can be extensively used in microwave antenna engineering, acoustics, and optoelectronics [10].

ACKNOWLEDGMENTS

I am grateful to Academician Yu.V. Gulyaev, Corresponding Members of the RAS L.D. Bakhrakh and V.I. Pustovoĭt, and Profs. E.G. Zelkin and Yu.S. Shifrin for discussion of the results of this study.

REFERENCES

1. V. F. Kravchenko, Dokl. Akad. Nauk **382** (2), 190 (2002) [Dokl. Phys. **47**, 51 (2002)].
2. V. F. Kravchenko and V. I. Pustovoĭt, Dokl. Akad. Nauk **386** (1), 38 (2002).
3. V. F. Kravchenko and M. V. Golubin, Élektromagn. Volny Élektron. Sistemy **7** (2), 25 (2002).
4. E. G. Zelkin and V. F. Kravchenko, Radiotekh. Élektron. (Moscow) **46** (8), 903 (2001).
5. R. C. Hansen, in *Microwave Scanning Antennas* (Academic, New York-London, 1964; Sov. Radio, Moscow, 1966), Vol. 1.
6. D. K. Barton and H. R. Vard, *Handbook of Radar Measurement* (Prentice-Hall, Englewood Cliffts, NJ, 1969; Sov. Radio, Moscow, 1976).
7. C. A. Balanis, *Antenna Theory. Analysis and Design* (Wiley, New York, 1997).
8. L. D. Bakhrakh and S. D. Kremenetskiĭ, *Synthesis of Emitting Systems. Theory and Methods of Calculation* (Sov. Radio, Moscow, 1974).
9. E. G. Zelkin and V. G. Sokolov, *Methods of Antenna Synthesis* (Sov. Radio, Moscow, 1980).
10. D. P. Morgan, *Surface-Wave Devices for Signal Processing* (Elsevier, Amsterdam, 1985).

Translated by V. Bukhanov

Doklady Physics, Vol. 48, No. 2, 2003, pp. 75–79. Translated from Doklady Akademii Nauk, Vol. 388, No. 5, 2003, pp. 611–615.

TECHNICAL PHYSICS

Explosion of a Bubble Curtain with a Combustible-Gas Mixture under the Action of a Pressure Pulse

Academician R. I. Nigmatulin, V. Sh. Shagapov, I. K. Gimaltdinov, and F. F. Akhmadulin

Received September 9, 2002

A bubble liquid with a combustible gas (e.g., water with either detonating-gas bubbles or a hydrocarbon–oxygen mixture) is an explosive. In this liquid, a detonation soliton with an amplitude of up to hundreds of atmospheres can arise under the action of a pressure pulse on the order of 10–20 atm [1]. The specific mass caloricity of such an explosive is lower by six or more orders of magnitude than for usual solid, liquid, and gaseous explosives. These low-caloric explosives are efficient means of amplifying and maintaining wave signals, as well as of temporarily elevating the pressure in local zones. In addition, in combustible liquids containing curtains with vapor–air bubbles, sharp shocks arising in the process of transportation can promote formation of detonation solitons leading to emergencies.

In this paper, in the two-dimensional setting schematically presented in Fig. 1, we consider an explosion of a finite-size curtain in a liquid under the action of a pressure pulse. Results are also given related to the dynamics of formation and separation of one-dimensional detonation waves due to nonlinear phenomena arising in the process of pressure-wave propagation through the inhomogeneity boundary in a bubble system inhomogeneous with respect to its volume content.

In order to describe the processes under discussion, we use the system of equations [2] written out in Lagrangian variables:

$$\frac{\partial p_\mathrm{l}}{\partial t} = \frac{C_\mathrm{l}^2\rho_\mathrm{l}^0}{1-\alpha_\mathrm{g}}\left[\frac{3\alpha_\mathrm{g}}{a}w - \left(\frac{\alpha_\mathrm{g}}{J} + \frac{\rho_{\mathrm{l}0}}{J^2\rho_\mathrm{l}^0}\right)\frac{\partial J}{\partial t}\right],$$

$$\frac{du}{dt} = -\frac{1}{J\rho}\left(\frac{\partial p_\mathrm{l}}{\partial x_0}\frac{\partial y}{\partial y_0} - \frac{\partial p_\mathrm{l}}{\partial y_0}\frac{\partial y}{\partial x_0}\right), \quad \frac{\partial x}{\partial t} = u,$$

$$\frac{dv}{dt} = -\frac{1}{J\rho}\left(\frac{\partial p_\mathrm{l}}{\partial y_0}\frac{\partial x}{\partial x_0} - \frac{\partial p_\mathrm{l}}{\partial x_0}\frac{\partial x}{\partial y_0}\right), \quad \frac{\partial y}{\partial t} = v,$$

$$\frac{\partial \alpha_\mathrm{g}}{\partial t} = \frac{3\alpha_\mathrm{g}}{a}w - \frac{\alpha_\mathrm{g}}{J}\frac{\partial J}{\partial t},$$

$$\frac{\partial p_\mathrm{g}}{\partial t} = -\frac{3\gamma p_\mathrm{g}}{a}w - \frac{3(\gamma-1)}{a}q, \tag{1}$$

$$\frac{\partial a}{\partial t} = w = w_R + w_A,$$

$$\frac{\partial w_R}{\partial t} = \left[\frac{p_\mathrm{g}-p_\mathrm{l}}{\rho_\mathrm{l}^0} - \frac{3}{2}w_R^2 - 4\nu_\mathrm{l}\frac{w_R}{a}\right]\frac{1}{a}, \quad w_A = \frac{p_\mathrm{g}-p_\mathrm{l}}{\rho_\mathrm{l}^0 C_\mathrm{l}\alpha_\mathrm{g}^{1/3}},$$

$$q = \mathrm{Nu}\lambda_\mathrm{g}\frac{T_\mathrm{g}-T_0}{2a}, \quad \mathrm{Nu} = \begin{cases}\sqrt{\mathrm{Pe}}, & \mathrm{Pe}\geq 100\\ 10, & \mathrm{Pe}<100,\end{cases}$$

$$\mathrm{Pe} = 12(\gamma-1)\frac{T_0}{|T_\mathrm{g}-T_0|}\frac{a|w|}{\kappa_\mathrm{g}}, \quad \kappa_\mathrm{g} = \frac{\lambda_\mathrm{g}}{c_\mathrm{g}\rho_\mathrm{g}},$$

$$\frac{T_\mathrm{g}}{T_0} = \frac{p_\mathrm{g}}{p_0}\left(\frac{a}{a_0}\right)^3,$$

$$J = \frac{\partial x}{\partial x_0}\frac{\partial y}{\partial y_0} - \frac{\partial x}{\partial y_0}\frac{\partial y}{\partial x_0},$$

$$\frac{\partial J}{\partial t} = \frac{\partial u}{\partial x_0}\frac{\partial y}{\partial y_0} - \frac{\partial u}{\partial y_0}\frac{\partial y}{\partial x_0} + \frac{\partial x}{\partial x_0}\frac{\partial v}{\partial y_0} - \frac{\partial x}{\partial y_0}\frac{\partial v}{\partial x_0}.$$

Here, a is the bubble radius; γ is the adiabatic index for the gas; p_i is the phase pressure; ρ_i^0 are the true phase densities; α_i is the phase volume content; q is the heat-exchange intensity; n is the number of bubbles per unit volume; w is the bubble radial velocity; x, y, and x_0, y_0 are Eulerian and Lagrangian coordinates, respectively; u and v are velocity components; T_0 = const is the temperature of the liquid; c_g and λ_g are, respectively, the gas heat capacity and gas thermal conduction; and J is the Jacobian of the passage from Eulerian to Lagrangian variables. The subscripts i = l, g correspond to parameters of the liquid phase and gas phase, respectively.

Sterlitamak Branch,
Academy of Sciences of Republic Bashkortostan,
pr. Lenina 3, Sterlitamak, 453103 Bashkortostan, Russia
e-mail: Iljas_g@mail.ru: famil@mail.rb.ru

1028-3358/03/4802-0075$24.00

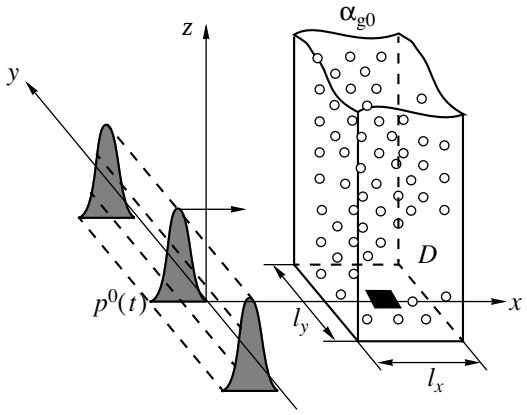

Fig. 1. Schematic image of the calculation region.

The process of inflammation of a combustible mixture in bubbles was taken into account in the framework of an instantaneous scheme. In accordance with this scheme, the gas temperature T_g increases stepwise by the quantity ΔT after the ignition temperature T_* has been attained. In this case, the parameter ΔT is responsible for the caloricity (caloric power) of the gas mixture in the bubbles. For $\alpha_g = 0$, an equation for acoustic waves in a pure liquid (free of bubbles) follows from set (1). In addition, in Lagrangian coordinates, the boundary of the bubble curtain, as well as the zone of various inhomogeneities, are immobile. This fact, in turn, makes it possible to use through calculation methods for the entire region.

Figure 2 illustrates the dynamics of the explosion process of a bubble column residing inside a semi-infinite liquid volume in the case of a pulse action across the boundary. The corresponding boundary conditions and initial conditions can be written out in the following form:

For $t = 0$,

$$p_l = p_g = p_0, \quad u = v = 0,$$
$$a = a_0, \quad w_R = 0, \quad T_g = T_0 \quad (x_0 > 0),$$

$$\alpha_g = \alpha_{g0}, \quad (x_0, y_0) \in Q, \quad \alpha_g = 0, \quad (x_0, y_0) \notin Q,$$

$$Q = \{(x_0, y_0) \mid x_{01} < x_0 < x_{02}, \quad y_{01} < y_0 < y_{02}\}.$$

For $x_0 = 0$,

$$p = p_0 + \Delta p_0 \exp\left[-\left(\frac{t - t_*}{t_0}\right)^2\right] \quad (t > 0).$$

In Figs. 2a, 2b, and 2c, profiles of gas pressure and temperature for different moments of time are presented. The pressure and temperature distributions are symmetric with respect to the straight line passing through the curtain center in parallel to the wave-propagation direction. Therefore, the calculation results are presented only for one of the half-planes separated by this line. As was shown in [3], the propagation of pulsed signals in a liquid containing a bubble curtain ($x_{02} - x_{01} = l_x$, $y_{02} - y_{01} = l_y$) in the case of a long-term [$t_* > \frac{l_x}{C}$, where $C = \left(\frac{\gamma p_0}{p_{10}\alpha_{g0}}\right)^{1/2}$ is the speed of sound in the bubble liquid] duration of the pulse has certain intrinsic features. In particular, at certain moments of time, the appearance of tower-shaped profiles of pressure and temperature with sufficiently high peak values is possible. Below, the situation is considered when this peak value attains the ignition temperature and, furthermore, the detonation process is developed. Figure 2a exhibits the distributions of pressure in the liquid and bubble temperature at the moment $t = 0.79$ ms. To this moment, the maximum gas temperature in bubbles is $T_g \simeq 450$ K but does not yet attain the ignition temperature $T_* = 600$ K. As is seen from Fig. 2b, corresponding to the moment $t = 0.81$ ms, the gas peak temperature has attained the ignition temperature, and the detonation wave has arisen and has begun to propagate in the curtain. To this moment, the maximum value of pressure of the liquid in the curtain is about $p_m = 4.2$ MPa. In Fig. 2c, distributions of pressure and temperature at the moment $t = 0.95$ ms, when the explosion wave has gone out of the curtain into the zone of the pure liquid, are shown. The maximum pressure in the explosion zone (in the curtain) has decreased down to $p_m = 2$ MPa. It is worth mentioning that the amplitude of the initiating pulse is $\Delta p_0 = 0.4$ MPa. Thus, this pulse is almost unnoticeable against the background of pressures realized in the curtain after the explosion. In Fig. 2d, calculated pressure oscillograms are shown for a sensor *D* residing in the center of the bubble curtain. The solid and dashed lines correspond to bubble curtains with a combustible mixture and inert gas, i.e., to the maximum pressures $p_m = 4.2$ and only 0.8 MPa, respectively.

In Fig 3a, diagrams of pressure and temperature in gas bubbles are presented for an evolving stepped wave in a bubble liquid inhomogeneous with respect to the gas volume content. In this case, the corresponding initial ($t = 0$) conditions are written out in the form

$$p_l = p_g = p_0, \quad u = 0, \quad a = a_0,$$
$$w_R = 0, \quad T_g = T_0 \quad (x_0 > 0),$$

$$\alpha_g = \alpha_{g0}^{(1)} \quad (x_0 \le x_{01}); \quad \alpha_g = \alpha_{g0}^{(2)} \quad (x_0 > x_{01});$$

and boundary conditions ($x_0 = 0$) in the form

$$p = p_0 + \Delta p_0 \quad (t > 0).$$

Numbers *1*, *2*, and *3* near curves in Fig. 3a correspond to the moments of time 2.3, 2.5, and 2.7 ms, respec-

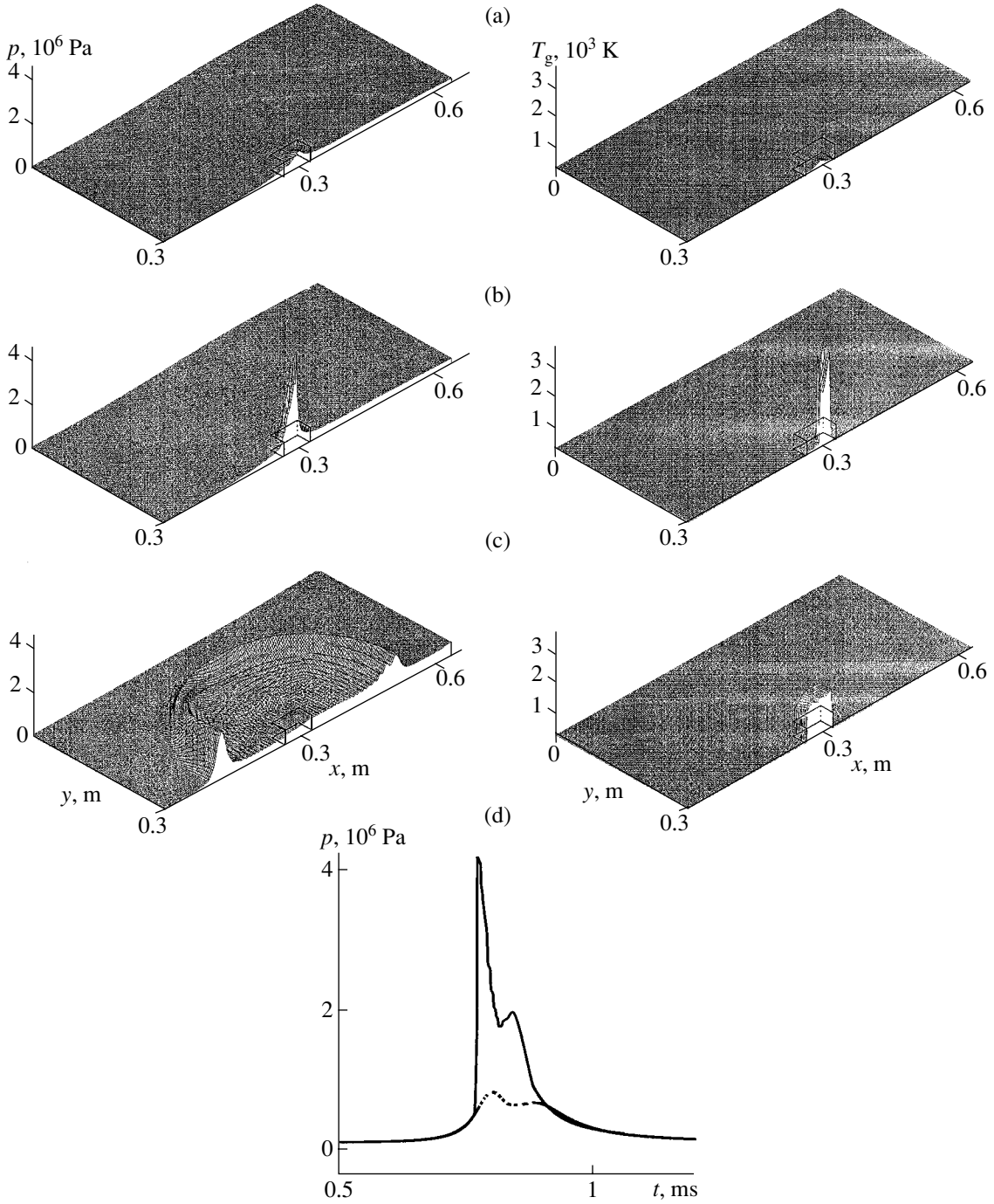

Fig. 2. (a–c) Profiles of gas pressure and temperature when exploding the bubble curtain with a combustible mixture of gases under the action of a pressure pulse; (d) calculated oscillograms of the pressure sensor D placed at the center of the bubble curtain. Parameters determining the initial states of both the system and the pulse are $p_0 = 10^5$ Pa; $\Delta p_0 = 0.4$ MPa; $T_0 = 300$ K; $a_0 = 1$ mm; $\alpha_{g0} = 0.01$; $T_* = 600$ K; $\Delta T = 3000$ K; $l_x = 0.06$ m; $l_y = 0.06$ m; $x_{01} = 0.27$ m; $t_* = 0.5$ ms; and $t_0 = 0.16$ ms.

tively. As is clearly seen, the shock wave with an amplitude of $\Delta p_0 = 0.3$ MPa is unable to initiate detonation in the first zone ($0 < x < x_{01}$). (For the given parameters of the mixture in the first zone, the amplitude of a wave capable of exciting detonation is $\Delta p \simeq 0.4$ MPa.) After the shock-wave front has reached the boundary between the zones in which the volume content decreases stepwise from $\alpha_{g0}^{(1)} = 0.1$ down to $\alpha_{g0}^{(2)} = 0.01$, nonlinear reflection occurs. The penetration of the pressure wave from a zone with a higher volume content to that with a lower one (i.e., respectively, from an

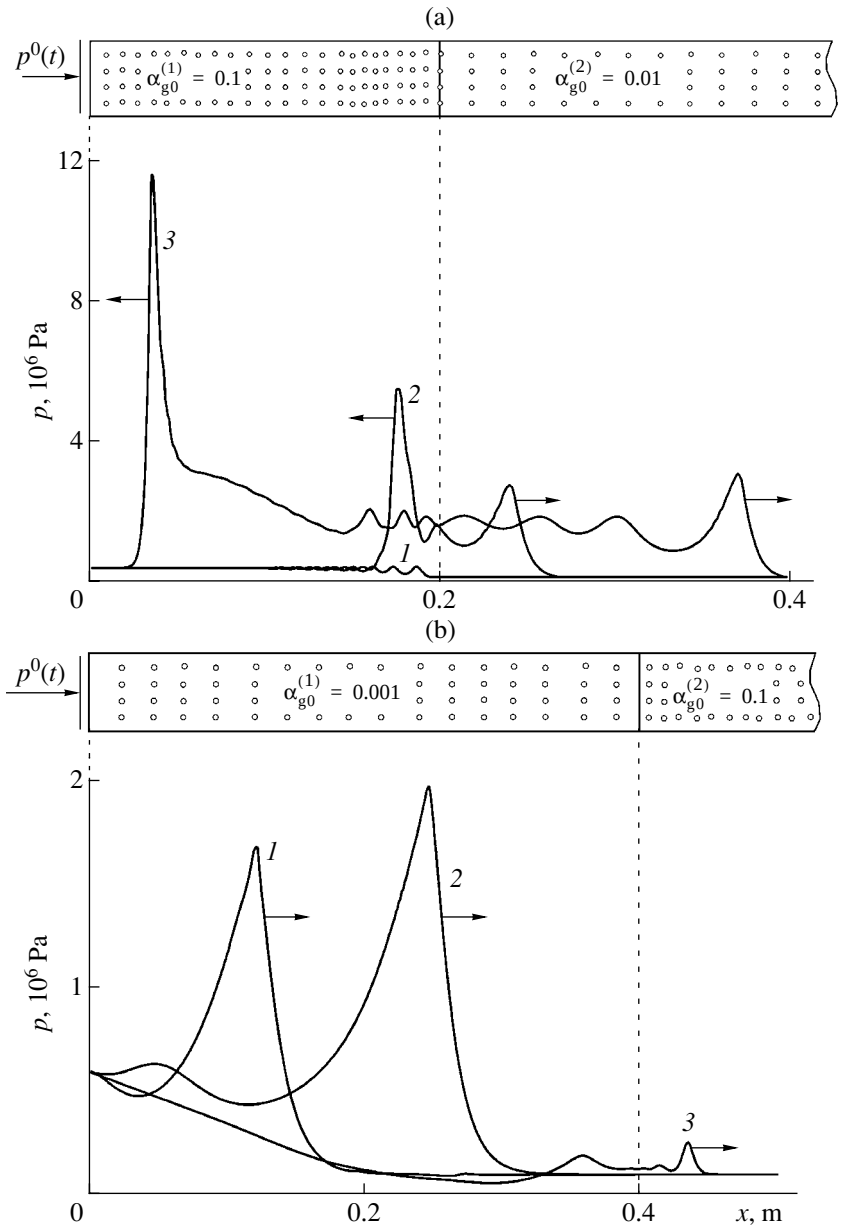

Fig. 3. Dynamics of a detonation soliton in a bubble liquid inhomogeneous with respect to the volume content. Parameters determining the initial states of the system and of the pulse are (a) $\Delta p_0 = 0.3$ MPa; $x_{01} = 0.2$ m; $\alpha_{g0}^{(1)} = 0.1$; $\alpha_{g0}^{(2)} = 0.01$; and (b) $\Delta p_0 = 0.5$ MPa; $x_{01} = 0.4$ m; $\alpha_{g0}^{(1)} = 0.01$; $\alpha_{g0}^{(2)} = 0.1$. Other parameters are the same as in Fig. 2.

acoustically softer to an acoustically stiffer zone) is accompanied by a multiple increase in the wave amplitude. By virtue of this fact, for bubbles corresponding to the boundary of a volume-content inhomogeneity, the ignition temperature T_* is attained and, thereby, the explosion center is formed. After this, the detonation wave is developed in both zones. In the first zone with the higher initial gas volume content, the amplitude of the detonation soliton (which propagates in the medium compressed by the initial shock wave) is several times higher than that in the second zone with the lower gas volume content.

In Fig. 3b, the calculation results are presented for the case when the detonation solution formed in the first zone having the gas volume content $\alpha_{g0}^{(1)} = 0.001$ interacts with the boundary of the zone having the higher gas volume content $\alpha_{g0}^{(2)} = 0.1$. Curves *1*, *2*, and *3* correspond to the moments of time 0.15, 0.25 and 1.0 ms. As is seen, when penetrating this boundary, the detona-

tion soliton and the shock wave that follows it are not capable of initiating detonation in the zone with a higher gas volume content (which is, generally speaking, a more caloric explosive). This is associated with the fact that the second zone (with $\alpha_{g0}^{(2)} = 0.1$) is acoustically a much softer medium than the first zone (with $\alpha_{g0}^{(1)} = 0.001$). Therefore, in the process of the interaction of the detonation soliton (as well as of the subsequent shock wave) with the boundary separating the zones, the inhomogeneity boundary for the gas volume content in fact plays the role of a free surface.

REFERENCES

1. A. V. Pinaev and A. I. Sychev, Fiz. Gorenia Vzryva **23** (6), 76 (1987).
2. R. I. Nigmatulin, V. Sh. Shagapov, and N. K. Vakhitova, Dokl. Akad. Nauk SSSR **304**, 1077 (1989) [Sov. Phys. Dokl. **34**, 98 (1989)].
3. R. I. Nigmatulin, V. Sh. Shagapov, I. K. Gimaltdinov, and M. N. Galimzyanov, Dokl. Akad. Nauk **378**, 763 (2001) [Dokl. Phys. **46**, 445 (2001)].

Translated by G. Merzon

Doklady Physics, Vol. 48, No. 2, 2003, pp. 80–83. Translated from Doklady Akademii Nauk, Vol. 388, No. 4, 2003, pp. 477–481.

MECHANICS

Asymmetric Behavior of a Sloping Spherical Shell under Finite Deflections

Corresponding Member of the RAS É. I. Grigolyuk and E. A. Lopanitsyn*

Received July 15, 2002

The current status of the theory and applications of calculating thin-wall constructions makes it possible to determine the stress–strain states of elastic shells of various shapes that are in equilibrium under external loads with an accuracy sufficient for engineering practice. This statement is true both for small deflections of shells and for finite and large deflections when the behavior of shells is described in various nonlinear mathematical models. The status of calculations of the stability of elastic shells is distinctly different. The same mathematical models considerably overestimate measured critical loads, and advanced skills are required to determine the critical loads with sufficient accuracy by semiempirical methods. This situation is most clear for well-studied elastic spherical shells.

The instability of a spherical shell was likely first observed by Bach [8] in 1902. In 1915, Zölly devoted his dissertation to the first calculation of the stability of thin elastic spherical shells in the linear approximation. Much later, in 1939, Boley and Seckler (see [11]) experimentally found that the critical pressure of a copper hemisphere was one-quarter the theoretical value calculated by Zölly's formula. Since that time, experimental information on the critical loads of spherical shells has increased continuously, and numerous calculations are carried out to determine the causes of discrepancy between measured and calculated data and to remove this discrepancy [7]. The authors of these calculations took into account the moment stress–strain state of a shell before the loss of stability, used geometrically nonlinear equations of the theory of shells, and considered shells with initial imperfections, including the imperfect shape of the shell, method of its fixing to the contour, possible elastoplastic deformation of the material of the shell, etc.

We consider a thin elastic sloping spherical shell that is rigidly fixed to the contour, has the modulus of elasticity E and Poisson's ratio ν, and is loaded by transverse pressure (see Fig. 1). The critical loads that are measured and calculated for this shell are shown in Fig. 2, where

$$q^* = [3(1-\nu^2)]^{1/2}\frac{qR^2}{2Eh^2}$$

is the dimensionless transverse pressure and

$$\mu = [12(1-\nu^2)]^{1/4}\frac{a^2}{(Rh)^{1/2}}$$

is the wall-thickness parameter. Lines *1* and *2* are, respectively, the upper q_+^* and lower q_-^* critical loads of the axisymmetrically deformed spherical shell as functions of its wall-thickness parameter as obtained by solving Marguerre's and Reissner's equations in various works. The circles in Fig. 2 are the upper critical loads measured in various experiments. The observed discrepancy between measured and calculated results is inevitably attributed to the imperfections of shells con-

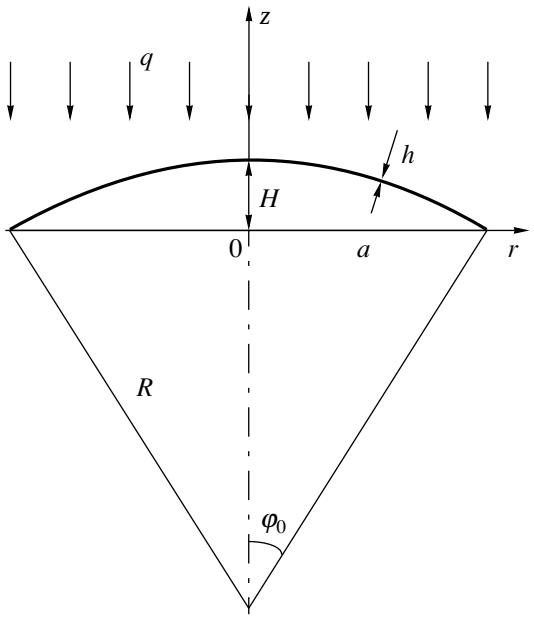

Fig. 1.

Moscow State Technical University "MAMI,"
Bol'shaya Semenovskaya ul. 38, Moscow, 105839 Russia
** e-mail: eal@mami.ru*

1028-3358/03/4802-0080$24.00

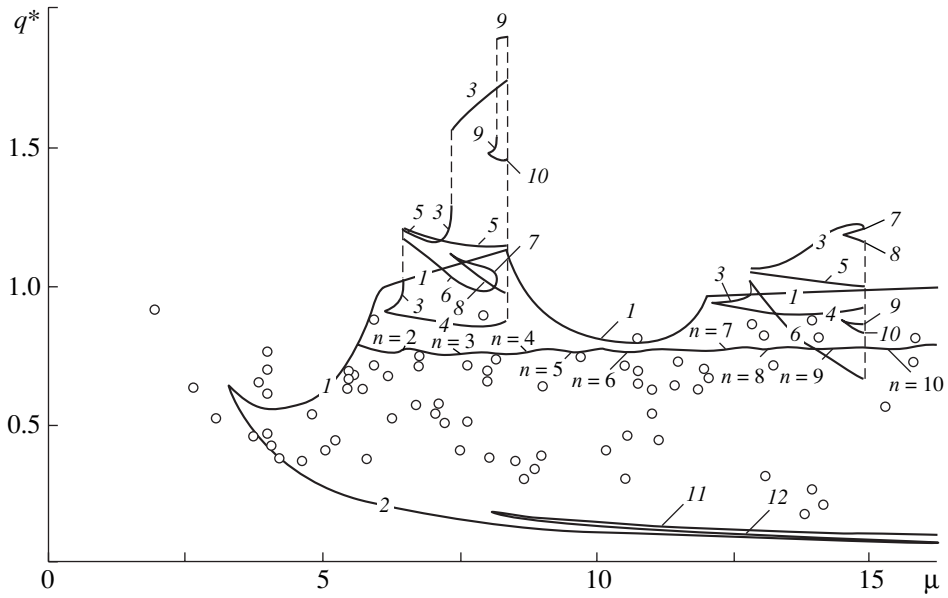

Fig. 2.

sidered in calculations. However, as was mentioned in [7], attempts to take into account the features of a real spherical shell were unsuccessful.

In particular, the shell shape explicitly deviates from the spherical shape, and this deviation is the primary factor affecting the critical load. However, its inclusion in the calculation reduces the upper critical load only by several tens of percent rather than by several times, as is necessary for agreement with experiment.

The high sensitivity of a spherical shell to imperfections is in particular illustrated by the solution to the axisymmetric formulation of the problem of the supercritical behavior of the sloping spherical shell under uniform transverse pressure. Mescall [12] calculated the entire stress–strain diagram for a $\mu = 8$ sloping shell both rigidly fixed and pivoted to the contour. More recently, we solved a similar problem for a rigidly fixed shell [6]. Some of our results are shown by lines *3–12* in Fig. 2. It is seen that the upper critical load of the shell for $\mu = 6$–8.5 and 13–15 can be reduced by introducing a small initial imperfection that is proportional to the shell deflection characteristic for lines *4* and *6*. However, this reduction is within the limits of ten percent achieved earlier.

Another way of solving the problem under consideration is analysis of the geometrically nonlinear behavior of a spherical shell with allowance for its nonaxisymmetric deformation. In 1960, one of us (É.I.G.) [1, 9] solved Marguerre's equations for a rigidly fixed sloping spherical shell subjected to uniform transverse pressure. Four years later, Huang [10] obtained quite reliable nonaxisymmetric critical loads for a sloping spherical shell rigidly fixed to the contour. The number $n = 2, 3, \ldots, 10$ along the line of the minimum nonaxisymmetric critical load in Fig. 2 is the number of waves in the shell circle. However, as is seen in Fig. 2, the nonaxisymmetric critical loads are also much larger than the experimental data.

In [13, 14], an acceptable compromise between calculated and measured data was found in the following approach. In addition to the deflections of the shell and corresponding loads, the authors measured the initial deflection that appeared in each unloaded shell after its fastening to the test bench. These data on the initial deflection, which is a random function of two variables, were used to calculate the snap of a shell loaded by uniform transverse pressure. As a result, the calculated upper critical loads for sloping spherical shells rigidly fixed to the contour agreed well with measured values.

That study again shows that the geometrically nonlinear equations of the theory of sloping shells, in particular Marguerre's equations, can be applied to calculate the critical loads of sloping spherical shells. The results of that study corroborate the high sensitivity of a sloping spherical shell to initial imperfections. Moreover, these results testify not only to the high sensitivity but also to the high selectivity of the shell to initial imperfections, because the critical loads differ considerably for various shapes of initial imperfections with approximately the same amplitudes. Therefore, the critical load of the shell is reduced only by those initial imperfections to which the shell is sensitive. Some forms of the initial imperfection of the shell can increase rather than decrease the critical load compared to the theoretical values for the ideal shell.

Continuing the above-reviewed investigations, this study aims to solve the problem of the geometrically nonlinear deformation of an elastic sloping spherical

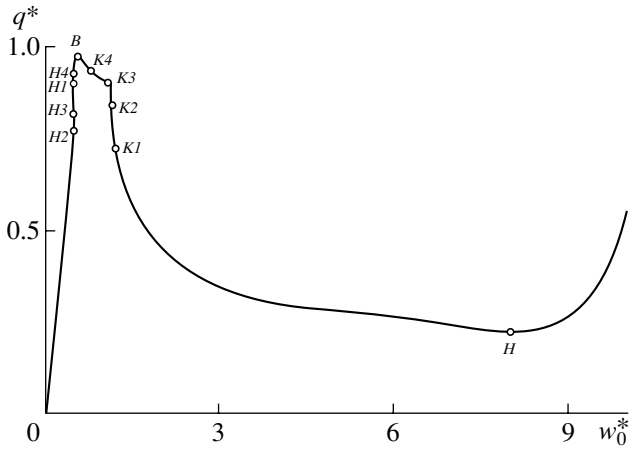

Fig. 3.

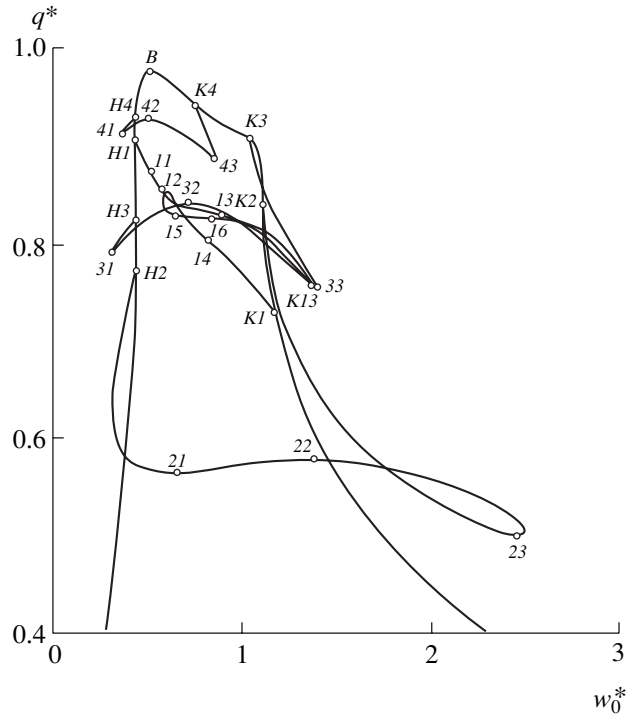

Fig. 4.

shell with allowance for both the nonaxisymmetric loss of stability and nonaxisymmetric supercritical behavior. Further, this solution is used to determine the initial shell imperfections that ensure the agreement of the calculated critical loads with experimental data.

The deformation of the shell in the subcritical state, in the state of stability loss, and in the supercritical state is described by Marguerre's equations in the asymmetric formulation in the polar coordinates r and θ. These equations are solved by the Rayleigh–Ritz method, where the radial u and circular v displacements, as well as the deflection w of the points of the middle surface of the spherical shell, are represented as the sum

$$u = \sum_{i=1}^{K_a} U_{ai} u_{ai}(r) + \sum_{i=1}^{K_n} U_{ni} u_{ni}(r) \cos n_i \theta,$$

$$v = \sum_{i=1}^{K_n} V_{ni} v_{ni}(r) \sin n_i \theta,$$

$$w = \sum_{i=1}^{K_a} W_{ai} w_{ai}(r) + \sum_{i=1}^{K_n} W_{ni} w_{ni}(r) \cos n_i \theta,$$

where subscripts "a" and "n" refer to axisymmetric and nonaxisymmetric components of the solution, respectively; U_{ai}, U_{ni}, V_{ni}, W_{ai}, and W_{ni} are the desired generalized displacements; and $u_{ai}(r)$, $u_{ni}(r)$, $v_{ni}(r)$, $w_{ai}(r)$, and $w_{ni}(r)$ are the basis functions expressed in terms of the Bessel functions according to the structure of the equations of shell equilibrium and boundary conditions. As a result, the problem reduces to a set of nonlinear algebraic equations with the matrix form $\mathbf{f}(\mathbf{x}) = \mathbf{0}$. Here, $\mathbf{f}$ is the vector whose components are the partial derivatives of the potential energy of shell deformation with respect to the generalized displacements and $\mathbf{x}$ is the vector whose components are the generalized displacements and dimensionless transverse load q^* according to equivalence between the variables of the solution.

The set of equations $\mathbf{f}(\mathbf{x}) = \mathbf{0}$ is solved by the method of continuation, where the algorithm described in [2, 3] is applied far from bifurcation points, whereas the methods proposed in [4, 5] are used to continue the solution near the bifurcation points.

Figure 3 shows the stress–strain curve for a sloping spherical shell that is deformed axisymmetrically and has $\mu = 6$, which can correspond to the shell with $\frac{R}{h} = 100$, $\varphi_0 = 19°$, and $\nu = 0.3$. The *OB* section and that to the right of the point *H* correspond to the stable axisymmetric equilibrium states of the shell, whereas the *BH* section corresponds to unstable states. At the point *B*, the shell loses its stability via snap in the first axisymmetric form, whereas at the point *H* the shell snaps back and returns to a shape close to the initial one.

When the shell can be deformed nonaxisymmetrically, bifurcation points *H1*, *H2*, *H3*, *H4*, *K1*, *K2*, *K3*, and *K4* appear on its stress–strain diagram (see Fig. 3). At the points *H1*, *H2*, *H3*, and *H4*, the loss of the Eulerian stability of the shell occurs with the formation of one, two, three, and four waves along the circle, respectively. These points are the initial points of the bifurcation branches of the stress–strain diagram, which correspond to unstable nonaxisymmetric equilibrium states of the shell. These branches are shown in Fig. 4. All the branches except the branch corresponding to one wave in the circle start at the points *H2*, *H3*, and *H4* and finish at the points *K2*, *K3*, and *K4*. The bifurcation branch describing states with one wave in the circle consists of two parts. Each part begins at the points *H1* and *K1* in

the axisymmetric section of the stress–strain diagram and finishes at the point *K13* in the bifurcation branch joining the points *H3* and *K3*. When leaving each bifurcation point in the stable section of the axisymmetric stress–strain diagram, nonaxisymmetric strains are superimposed on axisymmetric strains. When moving farther from the bifurcation point, these nonaxisymmetric stains become more pronounced. However, they become smaller when approaching the bifurcation point at the unstable section of the axisymmetric stress–strain diagram and vanish at the bifurcation point, where the shape of the shell becomes axisymmetric.

The above deformation pattern is characteristic only to a sloping spherical shell of the ideal shape. A real spherical shell always has small deviations from the ideal spherical shape and, under uniform transverse loading, is deformed nonaxisymmetrically according to the initial imperfect shape. Such a shell losses its stability through a snap. The comparison of the limiting loads characteristic for the limiting points *11*, *12*, …, *43* of the bifurcation branches of the ideal shell ($q^* = 0.5$–0.9, see Fig. 4) with the critical loads measured for the shell under consideration ($q^* = 0.37$–0.88, see Fig. 2) provides the following conclusion. In order for a small initial shape imperfection to be responsible for the observed decrease in the critical load, this imperfection must involve one or several components that are proportional to those shapes of the bent middle surface of the shell that are inherent in the stress–strain states at the limiting points *11*, *12*, …, *43*. The calculated critical load can likely be reduced to experimental data only in this case.

The above analysis of the nonaxisymmetric supercritical deformation of a sloping spherical shell implies that the observed spread of measured critical loads is primarily caused by the presence of small axisymmetric and nonaxisymmetric initial shape imperfections and is likely determined by the form, rather than magnitude, of these imperfections. The critical load must depend on the prevailing component of initial shell imperfections among the unstable supercritical equilibrium states found above. Thus, calculation with the introduction of small initial imperfections in the form of nonaxisymmetric supercritical equilibrium shapes must provide the spread observed for the measured critical loads.

REFERENCES

1. É. I. Grigolyuk, Izv. Akad. Nauk SSSR, Otd. Mekh. Mashinostr., No. 6, 68 (1960).
2. É. I. Grigolyuk and E. A. Lopanitsyn, Prikl. Mekh. Tekh. Fiz., No. 5, 95 (1990).
3. É. I. Grigolyuk and E. A. Lopanitsyn, Dokl. Akad. Nauk **335** (5), 582 (1994) [Phys. Dokl. **39**, 254 (1994)].
4. É. I. Grigolyuk and E. A. Lopanitsyn, Mat. Metody Fiz.-Mekh. Polya **41** (1), 35 (1998).
5. É. I. Grigolyuk and E. A. Lopanitsyn, in *Space of Life. To B. V. Raushenbakh's 85th Anniversary* (Nauka, Moscow, 1999), p. 192.
6. É. I. Grigolyuk and E. A. Lopanitsyn, Prikl. Mat. Mekh. **66** (4), 621 (2002).
7. É. I. Grigolyuk and V. I. Mamai, *Deformation Mechanics of Spherical Shells* (Izd. Mosk. Gos. Univ., Moscow, 1983).
8. C. Bach, VDI Z. **46** (10), 333 (1902).
9. E. I. Grigoljuk, in *Proceedings of the IUTAM Symposium on the Theory of Thin Elastic Shells, Delft, 1959* (Elsevier, Amsterdam, 1960), p. 112.
10. N.-C. Huang, AIAA J. **1** (4), 945 (1963); Trans. ASME, Ser. E **31** (3), 447 (1964).
11. Th. Karman and S. Tsien, J. Aeronaut. Sci. **7** (2), 43 (1939).
12. J. Mescall, AIAA J. **4** (11), 2041 (1966).
13. S. Yamada, K. Uchiyama, and M. Yamada, J. Nonlinear Mech. **18** (1), 37 (1983).
14. M. Yamada and S. Yamada, in *Collapse*, Ed. by J. M. T. Tompson and J. W. Hant (Cambridge Univ. Press, Cambridge, 1983), pp. 431–441.
15. R. Zölly, *Über ein Knickungsproblem an der Kugelschale. Promotionsarbeit* (Tech. Hochschule, Zürich, 1915).

Translated by R. Tyapaev

Doklady Physics, Vol. 48, No. 2, 2003, pp. 84–89. Translated from Doklady Akademii Nauk, Vol. 388, No. 4, 2003, pp. 482–487.

MECHANICS

On the Nonlinear Stability of Regular Vortex Polygons and Polyhedrons on a Sphere

L. G. Kurakin

Presented by Academician G.G. Chernyĭ October 30, 2002

Received October 30, 2002

1. INTRODUCTION

In this paper, we derive the necessary and sufficient conditions for the stability and instability of regular systems of point vortices on a sphere.

In 1885, Gromeka [1] treated a problem on motion of vortices on a sphere, which had been posed by Preobrazhenskiĭ. Later, the problem was studied from various viewpoints by many authors (see reviews [2, 3]). The importance of the model of point vortices for dynamic meteorology was pointed out in monograph [4]. The general Hamiltonian form for equations of motion of n point vortices on a sphere was derived in [5].

Bogomolov [6] was the first to analyze the stability problem for a configuration $V_R(n, \theta_0)$ of identical point vortices on a sphere with the radius R at a latitude θ_0 with the vortices located at the vertices of a regular n-gon that rotated with a constant angular velocity $\omega(\theta_0)$. As was shown in [6], the corresponding linearized system has solutions exponentially growing for $n \geq 7$, as well as for $n = 4, 5, 6$, provided that the latitude θ_0 lies within the range $J = (\theta_{*n}, \pi - \theta_{*n})$. In all other cases, there is only the power instability in the linear system, which is conventional and imminent for systems of such a kind. A linear analysis of the problem was independently performed in [2, 7] and generalized to systems of finite-size vortices in [7].

According to the well-known Lyapunov theorem, the equilibrium of a complete system is unstable when the linearized system is exponentially unstable. The question of the nonlinear instability and, in particular, of the possibility of suppressing the power instability of a linearized system by the action of nonlinear terms was posed in [6].

In the first section of this paper, we prove in the rigorous nonlinear formulation the stability of the stationary rotation of the vortex polygon $V_R(n, \theta_0)$ provided that $\theta_0 \notin J$ for $n = 4, 5, 6$. We treat the stability of stationary motion as a stability in the Routh sense [10, 11]. In the case of the latitude θ_0 lying at the end of the interval J, i.e., $\theta_0 = \theta_{*n}$ or $\pi - \theta_{*n}$, a special analysis of the stability is required to carry out the proof. It is interesting to analyze the stability for boundary values of the parameter in order to elucidate whether the boundary is "dangerous" or "safe" (in the Bautin sense [12]).

In the next sections, we analyze the stability for configurations of identical point vortices located in vertices of regular polyhedrons. The relation of this problem to meteorology was emphasized in monograph [2]. The equilibria of a system, which belong to continuous three-parameter sets of Tequilibria [i.e., to orbits of the $SO(3)$ symmetry group], correspond to regular vortex polyhedrons. Considering the vortex polyhedrons, we prove that a tetrahedron, octahedron, and icosahedron are stable, while a cube and dodecahedron are T unstable. In so doing, we regard the stability (instability) of a polyhedron as a stability (instability) of the corresponding $SO(3)$ orbit. In this case, the nonlinear stability problem turns out to be completely solvable in the linear approximation.

2. EQUATIONS OF MOTION FOR A SYSTEM OF POINT VORTICES ON A SPHERE

The motion of a system of n point vortices on a sphere is described by the equations

$$\frac{d\theta_k}{dt} = -\frac{1}{4\pi R^2}\sum_{j=1}^{n}{}' \kappa_j \frac{\sin\theta_j \sin(\varphi_k - \varphi_j)}{1 - \cos\gamma_{kj}},$$

$$\sin\theta_k \frac{d\varphi_k}{dt} = -\frac{1}{4\pi R^2} \tag{2.1}$$

$$\times \sum_{j=1}^{n}{}' \kappa_j \frac{\cos\theta_k \sin\theta_j \cos(\varphi_k - \varphi_j) - \sin\theta_k \cos\theta_j}{1 - \cos\gamma_{kj}},$$

$$\cos\gamma_{kj} = \cos\theta_k \cos\theta_j + \sin\theta_k \sin\theta_j \cos(\varphi_k - \varphi_j),$$

where $k = 1, 2, \ldots, n$ [5]. Here, the prime implies that the term with $j = k$ is omitted, R is the radius of the sphere, θ_k and φ_k are the spherical coordinates of the kth vortex ($0 < \theta_k < \pi$), κ_k is its strength, and γ_{kj} is the angle

Rostov State University,
ul. Zorge 5, Rostov-on-Don, 344104 Russia

between the radius vectors of the point vortices k and j with respect to the sphere center.

System (2.1) represents Hamilton equations with the Poisson bracket

$$\{U, V\} = \sum_{k=1}^{n} \frac{1}{\kappa_k}\left(\frac{\partial U}{\partial \varphi_k}\frac{\partial V}{\partial \cos\theta_k} - \frac{\partial U}{\partial \cos\theta_k}\frac{\partial V}{\partial \varphi_k}\right) \quad (2.2)$$

and the Hamiltonian

$$H = -\frac{1}{4\pi R^2}\sum_{1 \le j < k \le n} \kappa_j \kappa_k \ln(2R^2(1-\cos\gamma_{kj})). \quad (2.3)$$

These equations can be written out in the form

$$\frac{d\cos\theta_k}{dt} = \{\cos\theta_k, H\}, \quad \frac{d\varphi_k}{dt} = \{\varphi_k, H\}. \quad (2.4)$$

The system of equations (2.1) has four integrals

$$H,\ I_1 = R\sum_{k=1}^{n} \kappa_k \sin\theta_k \cos\varphi_k,$$
$$I_2 = R\sum_{k=1}^{n} \kappa_k \sin\theta_k \sin\varphi_k, \quad M = R\sum_{K=1}^{n} \kappa_k \cos\theta_k, \quad (2.5)$$

and its phase space is

$$Z = \{(\theta, \varphi) \in ((0, \pi) \times \mathbb{R}(\mathrm{mod}2\pi))^n : (\theta_j, \varphi_j) \neq (\theta_k, \varphi_k),\ j \neq k\}.$$

Here, $\theta = (\theta_1, \theta_2, \ldots, \theta_n)$ and $\varphi = (\varphi_1, \varphi_2, \ldots, \varphi_n)$.

System (2.1) is invariant with respect to an additive group L of real numbers $\mathbb{R}$: $h \longrightarrow L_h$, $h \in \mathbb{R}$. For each $h \in \mathbb{R}$ in the phase space Z, this group puts in correspondence a diffeomorphism L_h: $Z \longrightarrow Z$: $v \mapsto L_h v = (\theta, \varphi_1 + h, \varphi_2 + h, \ldots, \varphi_n + h)$ for an arbitrary point $v \in Z$. It is worth noting that the image $L(\mathbb{R}) = G^{\mathrm{tr}}$ is a one-parameter subgroup of the $SO(3)$ symmetry group that consists of rotations about the axis of the chosen spherical coordinate system. An arbitrary $SO(3)$ transformation is defined by three parameters. One of them is the angle of rotation about a certain axis, and two others define the angular position of the rotation axis.

We recall that motion called stationary if it can be presented as transformations of a certain one-parameter subgroup of a symmetry group for the equation given (see [8–11, 13, 14]).

We seek a stationary motion corresponding to the one-parameter group G^{tr} in the form

$$\theta_k = u_k, \quad \varphi_k = \omega t + v_k. \quad (2.6)$$

The corresponding equation in the variables $u_1, u_2, \ldots, u_n$ and $v_1, v_2, \ldots, v_n$, with $\omega \in \mathbb{R}$, is derived by substituting formulas (2.6) into Eqs. (2.1). Numerous examples of stationary motions for the system of equations (2.1) are considered in [6, 13, 14].

3. STABILITY OF A REGULAR VORTEX n-GON

We assume that all the vortices have the same strength κ. The time-independent solution in the form (2.6) corresponds to the vortex configuration $V_R(n, \theta_0)$:

$$\theta_k = \theta_0, \quad \varphi_k = \omega(\theta_0)t + \alpha(k-1),\ k = 1, 2, \ldots n,$$
$$\omega(\theta_0) = \frac{\kappa(n-1)}{4\pi R^2}\frac{\cos\theta_0}{\sin^2\theta_0}, \quad \alpha = \frac{2\pi}{n}. \quad (3.1)$$

The change of variables in system (2.1),

$$\theta_k = \theta_0 + r_k, \quad \varphi_k = \omega(\theta_0)t + \alpha(k-1) + p_k, \quad k = 1, 2, \ldots, n \quad (3.2)$$

reduces it to the equations of relative motion,

$$\frac{d\cos(\theta_0 + r_k)}{dt} = \{\cos(\theta_0 + r_k), E(\rho)\},$$
$$\frac{dp_k}{dt} = \{p_k, E(\rho)\} \quad (3.3)$$

with the relative (reduced) Hamiltonian

$$E(\rho) = H(\theta(r), \varphi(p)) - \omega(\theta_0)M(r),$$
$$M(r) = \kappa\sum_{k=1}^{n} \cos(\theta_0 + r_k), \quad (3.4)$$

where $\rho = (r, p) \in \mathbb{R}^{2n}$, $r = (r_1, r_2, \ldots, r_n)$, and $p = (p_1, p_2, \ldots, p_n)$. Stationary motion (3.1) corresponds to the continuous set Γ of equilibria of system (3.3). This set belongs to the straight line $\Gamma = \{(r, p) \in R^{2n}: r = 0, p_1 = \ldots = p_n\}$.

Certain different definitions of stability are also natural because of the evident and inessential instability of solution (3.1) in the Lyapunov sense, which is associated with the dependence of the angular velocity $\omega(\theta_0)$ on the latitude θ_0 (see, e.g., [8, 10, 11]). In other words, stationary solution (3.1) is stable in the Routh sense if the set Γ of equilibria for Eqs. (3.3) of relative motion is stable.

In order to substantiate the stability of stationary motion (3.1) in the Routh sense, it is sufficient to prove that the relative Hamiltonian $E(\rho)$ attains a transversally strict minimum on the set Γ of equilibria {see proposition (2.2) in [10, 11]}.

For any $n \ge 2$, the expansion into the Taylor series of the function $E(\rho)$ in the neighborhood of an arbitrary equilibrium belonging to the set Γ has the same form

$$E(\rho) = \frac{\kappa^2}{4\pi R^2}(E_0 + E_2(\rho) + E_3(\rho) + E_4(\rho) + \ldots), \quad (3.5)$$

where

$$E_2(\rho) = s^2(A_1 r, r) + (B_2 p, p),$$

$$E_3(\rho) = s^3\cos\theta_0(A_3 r, r^2) + s^2(B_4 p, r^2) + 2s^2(B_4 r, rp) - (B_4 p, p^2),$$

$$E_4(r, 0) = \left(\left(s^4 B_5 + \frac{1}{4}s^2 B_2 - \frac{1}{12}s^2\alpha_1 I\right)r^2, r^2\right) + \left(\left(s^4 B_6 - \frac{1}{3}s^2 B_1\right)r, r^3\right).$$

Here, $s = \sin^{-1}\theta_0$ and, for $k = 2, 3$,

$$r^k \stackrel{\text{def}}{=} (r_1^k, r_2^k, \ldots, r_n^k),$$
$$rp \stackrel{\text{def}}{=} (r_1 p_1, r_2 p_2, \ldots, r_n p_n),$$
$$\text{and } p^2 \stackrel{\text{def}}{=} (p_1^2, p_2^2, \ldots, p_n^2).$$

All the matrices B_j ($j = 1, 2, \ldots, 6$) are circulant matrices; i.e., they are polynomials of a cyclic matrix $\mathbb{C} = (c_{ij})_{ij=1}^n$ having nonzero elements only above its main diagonal ($c_{1,2} = \ldots = c_{n-1,n} = 1$) and ($c_{n,1} = 1$) in its lower left corner:

$$A_1 = \alpha_1 I + B_1, \quad A_3 = \alpha_3 I + B_3, \tag{3.6}$$
$$B_1 = b_1 I + B_0, \quad B_2 = b_2 I - B_0, \quad B_3 = b_3 I - B_0,$$
$$B_0 \stackrel{\text{def}}{=} \sum_{m=1}^{n-1} a_m \mathbb{C}^m, \quad B_4 = 2\sum_{m=1}^{n-1} \sin\frac{2\pi m}{n} a_m^2 \mathbb{C}^m,$$
$$B_5 = b_5 I + \frac{3}{2}\sum_{m=1}^{n-1} a_m^2 \mathbb{C}^m, \quad B_6 = -2\sum_{m=1}^{n-1} \cos\frac{2\pi m}{n} a_m^2 \mathbb{C}^m.$$

Here,

$$a_m = \frac{1}{2}\frac{1}{1-\cos\frac{2\pi m}{n}}, \quad b_1 = \frac{1}{12}(n-1)(5-n),$$
$$b_2 = \frac{1}{12}(n^2-1),$$
$$b_3 = \frac{1}{12}(n-1)(n-3),$$
$$b_5 = \frac{1}{1440}(n-1)(n^3+n^2-109n+251),$$
$$\alpha_1 = \frac{1}{2}(n-1)\cos^2\theta_0, \quad \alpha_3 = -\frac{1}{6}(n-1)\sin^2\theta_0.$$

The eigenvalues λ_{1k} and λ_{2k} of the matrices A_1 and B_2 are

$$\lambda_{1k} = \frac{1}{2}(n-1)(1+\cos^2\theta_0) - \frac{1}{2}k(n-k),$$
$$\lambda_{2k} = \frac{1}{2}k(n-k), \quad 1 \le k \le n.$$

The critical value of the latitude $\theta_0 = \theta_{*n}$ is determined by the conditions

$$\theta_{*2} = \theta_{*3} = \frac{\pi}{2}, \quad \cos^2\theta_{*4} = \frac{1}{3}, \quad \cos^2\theta_{*5} = \frac{1}{2}, \quad \cos^2\theta_{*6} = \frac{4}{5}. \tag{3.7}$$

The following theorem is a basis of the linearization method in the stability problem for the vortex n-gons $V_R(n, \theta_0)$ with $n \ge 2$ in the case of noncritical values of the T latitude ($\theta_0 \ne \theta_{*n}$). In what follows, instability implies the transversal instability of the three-dimensional set of stationary motions corresponding to $SO(3)$ symmetry in addition to the lack of stability in the Routh sense.

Theorem 3.1. *Stationary rotation* (3.1) *of a regular vortex n-gon on a sphere is stable in the Routh sense if two or three vortices lie out of the sphere equator* $\left(n = 2, 3; \theta_0 \ne \frac{\pi}{2}\right)$ *or if the following conditions are simultaneously satisfied*: (*a*) $4 \le n \le 6$ *and* (*b*) $\cos\theta_0 < \cos\theta_{*n}$.

Such a rotation is unstable if condition (*b*) *is violated, i.e., if* $\cos\theta_0 > \cos\theta_{*n}$ ($n = 4, 5, 6$) *or if* $n \ge 7$.

Proof repeats the substantiation of the linearization method in the stability problem for a regular vortex n-gon in a plane (see Theorem 3.1 in [10, 11]).

The proof of the nonlinear stability of a regular vortex triangle on a sphere, including the case of the triangle on the sphere equator, was given in [9]. It is based on the energy–moment method and uses the results obtained in [8]. Borisov and Kilin [15] introduced the concept of relative stability of a regular vortex n-gon and proved the corresponding analog of Theorem 3.1. Nonlinear analysis of the stability of $2N$ point vortices on a sphere (N vortices with strength $\kappa_1 = 1$ and the rest with strength $\kappa_2 = -1$) was carried out in [14].

In the critical case of $\theta_0 = \theta_{*n}$ ($2 \le n \le 6$), the matrix A_1 has the zero eigenvalue simple for even n and twofold degenerate for odd n. Because of this, we have to allow for the third-order and higher order terms in expansion (3.5).

The circulant matrices A_1 and B_2 have the common basis $\{h_1, h_2, \ldots, h_n\}$ in the space $\mathbb{R}^n$:

$$h_m = (1, \cos(m\alpha), \ldots, \cos((n-1)m\alpha)),$$
$$h_{n-l} = (0, \sin(l\alpha), \ldots, \sin((n-1)l\alpha)),$$
$$h_n = (1, 1, \ldots, 1), \quad \alpha = \frac{2\pi}{n},$$
$$m = 1, 2, \ldots, n-1-\left[\frac{n-1}{2}\right],$$
$$l = 1, 2, \ldots, \left[\frac{n-1}{2}\right].$$

Thus, $A_1 h_k = \lambda_{1k} h_k$ and $B_2 h_k = \lambda_{2k} h_k$, $k = 1, 2, \ldots, n$.

The decompositions of the vectors r and p in this basis have the form

$$r = \sum_{k=1}^{n} \xi_k h_k, \quad p = p_\perp + \zeta_n h_h, \quad p_\perp = \sum_{k=1}^{n-1} \zeta_k h_k.$$

The Hamiltonian $E(\rho)$ is independent of the variable ζ_n, and, in the neighborhood of the set Γ, its asymptotic behavior takes the form

$$E(\rho) = \frac{\kappa^2}{4\pi R^2}(E_0 + \mathbb{S}_n(\hat{r}, \tilde{r}, p_\perp) + o(|\hat{r}|^4 + |\tilde{r}|^2 + |p_\perp|^2)), \quad (\hat{r}, \tilde{r}, p_\perp) \longrightarrow 0. \tag{3.8}$$

Here, we introduce the vectors $\hat{r} \in \ker A_1$ and $\tilde{r} \in \mathbb{R}^n \ominus \ker A_1$, with $r = \hat{r} + \tilde{r}$, the function $\mathbb{S}_n$ for $n = 4$, 5, 6 being determined by the equalities

$$2\mathbb{S}_4 = 3\xi_1^2 + 3\xi_3^2 + 24\xi_4^2 + 6\zeta_1^2 + 16\zeta_2^2 + 6\zeta_3^2 + 15\xi_2^4, \tag{3.9}$$

$$\frac{1}{5}\mathbb{S}_5 = \xi_1^2 + \xi_4^2 + 6\xi_5^2 + \zeta_1^2 + \frac{3}{2}\zeta_2^2 + \frac{3}{2}\zeta_3^2 + \zeta_4^2 + \frac{3}{2}\xi_1\xi_2^2 + \xi_2^2\xi_5 + 2\xi_2^2\zeta_4 - 3\xi_2\xi_3\xi_4 + 4\xi_2\xi_3\zeta_1 - \frac{3}{2}\xi_1\xi_3^2 + \xi_3^2\xi_5 - 2\xi_3^2\zeta_4 + \frac{41}{16}(\xi_2^2 + \xi_3^2)^2, \tag{3.10}$$

$$\frac{2}{3}\mathbb{S}_6 = 20\xi_1^2 + 5\xi_2^2 + 5\xi_4^2 + 20\xi_5^2 + 90\xi_6^2 + 5\zeta_1^2 + 8\zeta_2^2 + 18\zeta_3^2 + 8\zeta_4^2 + 5\zeta_5^2 + 140\xi_3^2\xi_6 + 510\xi_3^4. \tag{3.11}$$

Taking arbitrary $x \in \mathbb{R}$, we divide the polynomial $\mathbb{S}_5$ into the terms

$$\frac{1}{5}\mathbb{S}_5 = \mathbb{S}_{51} + \mathbb{S}_{52} + \frac{3}{2}\zeta_2^2 + \frac{3}{2}\zeta_3^2, \tag{3.12}$$

$$\mathbb{S}_{51} = \xi_1^2 + 6\xi_5^2 + \zeta_4^2 + \frac{3}{2}\gamma_2\xi_1 + \gamma_2\xi_5 + 2\gamma_2\zeta_4 - \frac{3}{2}\gamma_3\xi_1 + \gamma_3\xi_5 - 2\gamma_3\zeta_4 + \frac{41}{16}\gamma_2^2 + \frac{41}{16}\gamma_3^2 - 2x\gamma_2\gamma_3,$$

$$\mathbb{S}_{52} = \xi_4^2 + \zeta_1^2 - 3\beta\xi_4 + 4\beta\zeta_1 + \left(\frac{41}{8} + 2x\right)\beta^2,$$

where $\gamma_2 = \xi_2^2$, $\gamma_3 = \xi_3^2$, and $\beta = \xi_2\xi_3$. In the case of $x \in \left(\frac{9}{16}, \frac{119}{48}\right)$, both the quadratic forms $\mathbb{S}_{51}$ and $\mathbb{S}_{52}$ are positive definite, because the conditions of the Sylvester criterion are satisfied for all $\gamma_2, \gamma_3 \in \mathbb{R}$ but not only for positive values, which we need.

The polynomial K has the form $K = 9\xi_6^2 + 14\xi_3^2\xi_6 + 51\xi_3^4$; therefore, the polynomial $\mathbb{S}_6$ is positive definite.

The following theorem is valid.

Theorem 3.2. *In the critical case of* $\theta_0 = \theta_{*n}$, *for* $n = 4, 5, 6$, *stationary rotation* (3.1) *of a regular vortex n-gon is stable in the Routh sense* [*see* (3.7)].

4. STABILITY OF REGULAR VORTEX POLYHEDRONS

Let n point vortices ($n = 4, 6, 8, 12, 20$) be positioned at the vertices of a regular polyhedron $(\theta_{j0}, \varphi_{j0})$ ($j = 1, 2, \ldots, n$) on a sphere with the radius R (see Table 1). Then, the constant solution

$$\theta_k = \theta_{k0}, \quad \varphi_k = \varphi_{k0}, \quad k = 1, 2, \ldots, n \tag{4.1}$$

to Eq. (2.1) corresponds to this vortex configuration.

Replacing the variables

$$\theta_k = \theta_{k0} + r_k, \quad \varphi_k = \varphi_{k0} + p_k, \quad k = 1, 2, \ldots, n \tag{4.2}$$

and expanding Hamiltonian (2.2) into a series in the neighborhood of the point $(r, p) = (0, 0)$, we arrive at the expression

$$H(\theta(r), \varphi(p)) = \frac{\kappa^2}{4\pi R^2 m_n}(H_0 + A_n(\rho, \rho) + \ldots). \tag{4.3}$$

Here, the ellipsis stands for the third-order and higher order terms; H_0 is the zero-order term; A_n is the matrix; and m_n is the scale factor introduced for simplifying Table 2 ($m_4 = 8$, $m_6 = 4$, $m_8 = 8$, $m_{12} = 8$, and $m_{20} = \frac{8}{\sqrt{3}}$).

Table 1. Angular coordinates for vertices of regular polyhedrons: (*1*) tetrahedron, (*2*) octahedron, (*3*) cube, (*4*) icosahedron, and (*5*) dodecahedron, *n* is the number of vertices.

No.	*n*	Angular coordinates of the vertices of the polyhedrons: $(\theta_{j0}, \varphi_{j0})$, $j = 1, 2, \ldots, n$
1	4	(ν, β), $(\nu_1, 3\beta)$, $(\nu, 5\beta)$, $(\nu_1, 7\beta)$, $\beta = \frac{\pi}{4}$, $\nu = \arccos\frac{1}{\sqrt{3}}$, $\nu_1 = \pi - \nu$
2	6	$(\gamma, 0)$, (γ, π), (β, γ), $(\beta, 3\gamma)$, $(3\beta, 3\gamma)$, $(3\beta, \gamma)$, $\gamma = \frac{\pi}{2}$
3	8	(ν, β), $(\nu, 3\beta)$, $(\nu, 5\beta)$, $(\nu, 7\beta)$, (ν_1, β), $(\nu_1, 3\beta)$, $(\nu_1, 5\beta)$, $(\nu_1, 7\beta)$
4	12	(μ, γ), (μ_1, γ), $(\mu_1, 3\gamma)$, $(\mu, 3\gamma)$, $(\eta, 0)$, $(\eta_1, 0)$, (η_1, π), (η, π), (γ, π), $(\gamma, 2\pi - \eta)$, $(\gamma, \pi + \eta)$, (γ, η_1), $\mu = \arccos a$, $\mu_1 = \pi - \mu$, $\eta = \arccos(ab)$, $\eta_1 = \pi - \eta$, $a = \frac{1}{\sqrt{1 + b^2}}$, $b = \frac{1}{2}(\sqrt{5} + 1)$
5	20	$(\gamma, 2\pi - \phi)$, (γ, ϕ), $(\gamma, \pi + \phi)$, (γ, ϕ_1), $(\nu, 5\beta)$, $(\nu_1, 3\beta)$, $(\nu_1, 7\beta)$, (ν, β), $(\psi, 3\gamma)$, (ψ_1, γ), $(\psi_1, 3\gamma)$, (ψ, γ), $(\nu, 7\beta)$, (ν_1, β), $(\nu_1, 5\beta)$, $(\nu, 3\beta)$, (ϕ_1, π), (ϕ, π), $(\phi, 0)$, $(\phi_1, 0)$, $\psi = \arccos\frac{b}{\sqrt{3}}$, $\phi = \arccos\frac{d}{\sqrt{3}}$, $\psi_1 = \pi - \psi$, $\phi_1 = \pi - \phi$, $d = \frac{\sqrt{5} - 1}{2}$

The linearization of system (2.1) for equilibrium (3.13) results in the equation

$$\dot{\rho} = \frac{\kappa}{4\pi R^2 m_n} L_n \rho = \frac{\kappa}{4\pi R^2 m_n} \begin{pmatrix} 0 & I \\ -D & 0 \end{pmatrix} \mathrm{grad}(A_n \rho, \rho), \qquad (4.4)$$

where $D = \mathrm{diag}(d_1, d_2, \ldots, d_n)$ and $d_k = \sin^{-1}\theta_{k0}$.

Let $P_n(\lambda) = \det(A_n - \lambda I_{2n})$ and $Q_n(\lambda^2) = \det(L_n - \lambda I_{2n})$ be characteristic polynomials of the matrices A_n and L_n, respectively (see Table 2). The polynomials of degree eight, namely, $R_2(\lambda^2)$, $R_3(\lambda^2)$, and $R_4(\lambda^2)$ entering into Q_{20}, are not presented here, because they are very awkward. The polynomial $R_1(x)$ of degree five has nonzero roots with a nonnegative real part, because its coefficients are of different sign. Therefore, the polynomial $R_1(\lambda^2)$ has roots in the right half-plane. As follows from our calculations, they are $\lambda_{1*} \approx 9.9704$ and $\lambda_{2*} \approx 11.8938$. The polynomial $Q_8(\lambda^2)$ also has a twofold positive root $\lambda_{3*} = 2\sqrt{5}\sqrt[4]{6}$. Each of the polynomials P_4, P_6, and P_{12} has a threefold zero root with positive other roots. This can be proved for the polynomial P_{12} when imposing, e.g., the Hurwitz criterion on its coefficients after replacing $\lambda \longrightarrow -\lambda$.

Equilibrium (4.1) belongs to the continuous three-parameter set Γ_n [an orbit of the $SO(3)$ symmetry

Table 2. Characteristic polynomials P_n and Q_n of the matrices A_n and L_n

No.	$P_n(\lambda)$ or $Q_n(\lambda^2)$
1	$P_4(\lambda) = \lambda^3(\lambda - 9)^2(\lambda - 6)(\lambda - 12)(\lambda - 4)$
2	$P_6(\lambda) = \lambda^3(\lambda - 2)^2(\lambda - 6)^2(\lambda - 10)^2(\lambda - 1)(\lambda - 5)(\lambda - 8)$
3	$Q_8(\lambda^2) = \lambda^6(\lambda^2 + 64\sqrt{6})(\lambda^2 - 45 + 82\sqrt{6})^2(\lambda^2 - 20\sqrt{6})^2$
4	$P_{12}(\lambda) = \lambda^3 T_+(\lambda) T_-(\lambda) U_+(\lambda) U_-(\lambda) T_1(\lambda) T_2(\lambda) T_3(\lambda) T_4(\lambda)$, $T_\pm(\lambda) = \lambda^3 - (65 \pm 17b_0)\lambda^2 + (1092 \pm 716b_0)\lambda - 2992(1 \pm b_0)$, $U_\pm(\lambda) = \lambda^2 - (39 \pm 3a_0)\lambda + 260 \pm 20a_0$, $T_1(\lambda) = 5\lambda^3 - 140\lambda^2 + 576\lambda - 544$, $T_2(\lambda) = (\lambda - 4)(\lambda - 34)(\lambda - 44)$, $T_3(\lambda) = \lambda^2 - 32\lambda + 120$, $T_4(\lambda) = (\lambda - 10)(\lambda - 40)^2$, $a_0 = \sqrt{5}$, $b_0 = a_0^{-1}$
5	$Q_{20}(\lambda^2) = \lambda^6 R_1(\lambda^2) R_2(\lambda^2) R_3(\lambda^2) R_4(\lambda^2)$, $R_1(\lambda^2) = \lambda^{10} + 3(903c_0 - 82d_0 + 506e_0 + 483) f_0^2 \lambda^8 + (501293c_0 + 1009454d_0 + 456918e_0 + 1652685) f_0^3 \lambda^6$ $- 31(7063201c_0 + 11390547d_0 + 5542581e_0 - 5875443) f_0^3 \lambda^4 - 758229(31875c_0 - 24435d_0 + 27074c_0$ $- 12886) f_0^2 \lambda^2 + 31^3 263^2 270$, $c_0 = \sqrt{2}\sqrt{3}$, $d_0 = \sqrt{2}\sqrt{5}$, $e_0 = \sqrt{3}\sqrt{5}$, $f_0 = \frac{1}{4}$

group] of equilibria of system (2.1). Therefore, the kernels of matrices A_n and L_n are threefold.

Theorem 4.1. *The three-dimensional sets* Γ_n *of equilibria of system* (2.1) *are stable when they correspond to a vortex tetrahedron, octahedron, and icosahedron but unstable in the cases of a cube and dodecahedron* (n = 4, 6, 12, 8, *and* 20, *respectively*).

Proof. In the problem under consideration, the component transversal to the set Γ_n of equilibria of system (2.1) can be separated and becomes independent of the tangential component. In the cases of n = 4, 6, 12, all the eigenvalues of the matrix A_n are positive except for the threefold zero eigenvalue. Hence, Hamiltonian $H(\rho)$ attains the transversally strict minimum on the compact set Γ_n of equilibria. Thus, the set is stable. In the two other cases (n = 8, 20), the conclusion of Theorem (4.1) on the instability of the set Γ_n and, moreover, of its isolated elements follows from the general Lyapunov theorem, because the linearized system is exponentially unstable.

ACKNOWLEDGMENTS

The author is grateful to V.I. Yudovich for his attention to this study. The work was supported by the Russian Foundation for Basic Research, project nos. 00-15-96188, 01-01-22002, and 02-01-00337.

REFERENCES

1. I. S. Gromeka, *Collected Papers* (Izd. Akad. Nauk SSSR, Moscow, 1952).
2. A. V. Borisov and I. S. Mamaev, *Poisson's Structures and Lee Algebras in Hamiltonian Mechanics* (Izd. Udmurt. Univ., Izhevsk, 1999).
3. P. K. Newton, *The N-Vortex Problem. Analytical Techniques. Applied Mathematical Sciences* (Springer, New York, 2001), Vol. 145.
4. N. E. Kochin and B. A. Izvekov, *Dynamic Meteorology* (Red. Izd. Otd. TsUEGMS, Leningrad, 1935), Part 1.
5. V. A. Bogomolov, Izv. Akad. Nauk SSSR, Mekh. Zhidk. Gaza, No. 6, 57 (1977).
6. V. A. Bogomolov, Fiz. Atm. Okeana **15** (3), 243 (1979).
7. L. M. Polvani and D. G. Dritschel, J. Fluid Mech. **255**, 35 (1993).
8. G. Patrick, J. Geom. Phys. **9**, 111 (1992).
9. S. Pekarsky and J. Marsden, J. Math. Phys. **39**, 5894 (1998).
10. L. G. Kurakin and V. I. Yudovich, Dokl. Akad. Nauk **384** (4), 476 (2002) [Dokl. Phys. **47**, 465 (2002)].
11. L. G. Kurakin and V. I. Yudovich, Chaos **12**, 574 (2002).
12. N. N. Bautin, *Behavior of Dynamic Systems Near the Boundary of the Stability Region* (Gostekhizdat, Moscow–Leningrad, 1984).
13. C. Lim, J. Montaldi, and M. Roberts, Physica D **148**, 97 (2001).
14. F. Laurent-Polz, Nonlinearity **15** (1), 143 (2002).
15. A. V. Borisov and A. A. Kilin, Reg. Ch. Dynamics **5** (2), 189 (2000).

Translated by V. Chechin

Doklady Physics, Vol. 48, No. 2, 2003, pp. 90–93. Translated from Doklady Akademii Nauk, Vol. 388, No. 5, 2003, pp. 616–619.

MECHANICS

Hydrodynamic Mechanism of Bleaching a Strongly Absorbing Liquid with a Laser Pulse

A. N. Kucherov

Presented by Academician G.G. Chernyĭ October 23, 2002

Received October 24, 2002

In the present paper, the hydrodynamic divergence of a liquid as a result of strong absorption of laser-pulse energy is studied, and the possibility of bleaching water is considered. Diagrams for the heating and motion of the liquid in the enthalpy–pressure plane are also given for a wide energy range of an yttrium–erbium laser pulse. Dependences for the density, pressure, temperature, and velocity of water on the coordinates and time are obtained. Theoretical estimates for the magnitude of the transmission (transparency) are compared with available experimental data.

In experimental studies of laser-pulse propagation through a layer of a strongly absorbing liquid, a bleaching effect (i.e., an increase in the transparency), particularly in water, glycerin, ethanol, methanol, etc., was discovered in [1–5]. In these experiments, high temperatures (>2000 K) and high pressures (~20 kbar) were attained, and a variation of the refractive index was observed. Several possible mechanisms explaining the bleaching effect were suggested, e.g., the absorption saturation, the liquid–vapor phase transition, the absorption-spectrum shift due to the breakdown of hydrogen bonds, and the broadening of the absorption band. The possibility of density reduction due to the removal of the substance away from the zone being irradiated was also indicated. However, none of these causes has gained theoretical substantiation until now.

The difficulties inherent in theoretical calculations of laser-radiation propagation in liquids are associated with the appearance of discontinuities, shock waves, and vapor bubbles. The other arguments are the incompleteness of data required for composing the equation of state for a liquid and the absence of information concerning the complex refractive index within a region of high energies, high intensities, high temperatures, and high pressures. At the same time, as we show below, the available rich experimental data make it possible, under the assumption of invariant quantum mechanical properties, to substantiate the last of the above hypotheses using numerical solutions.

We now analyze the heating and divergence of a thin layer $\Delta z \sim \alpha^{-1}$ of the liquid with the absorption coefficient α as a result of the strong absorption of the energy E of a laser pulse with a duration τ. Time-dependent equations written out in cylindrical coordinates for the conservation of mass, momentum, and energy (Navier–Stokes equations) were obtained by the large-particle method [6]. The equations of state for water were taken in the form of the dependence of the internal energy ε and of pressure p on the density ρ and temperature T with the use of the thermodynamic function of the free energy $F(\rho, T)$ [7, 8]: $\varepsilon = F - T\left(\frac{\partial F}{\partial T}\right)_\rho$, $p = \rho^2\left(\frac{\partial F}{\partial \rho}\right)_T$. The transport coefficients and the speed of sound can be found in [9–11]. The heat source was given in the form

$$q(r, t) = \rho(r, t)\frac{\alpha E}{\rho_0 \tau} f\left(\frac{t}{\tau}\right)\exp\left[-\frac{\alpha\rho}{\rho_0}\Delta z - \left(\frac{r}{r_0}\right)^2\right]. \quad (1)$$

Here, ρ and ρ_0 are the current density of the liquid and the value of the initial unperturbed density; S is the cross-sectional area of the laser beam; and r_0 is its (exponential) radius. The temporal shape of the laser pulse was given in the form of a linear segment with the extent $\frac{\tau}{k}$ (k = 2–5) with the subsequent decrease obeying the Gaussian law. The conditions of continuity at $t = \frac{\tau}{k}$ and of the normalization of the function $f\left(\frac{t}{\tau}\right)$, namely, $\int_0^\infty f(x)dx = 1$, were used. The calculation-mesh domain was chosen to be equal to $0 \le r \le 20r_0$. The main amount of the solutions was obtained for the numbers of spatial nodes and of time steps, which were equal to 401 and several thousand, respectively. The error of the

Zhukovskiĭ Central Aerohydrodynamic Institute (TsAGI), Zhukovskiĭ, Moscow oblast, 140180 Russia
e-mail: ank@aerocentr.msk.su

1028-3358/03/4802-0090$24.00

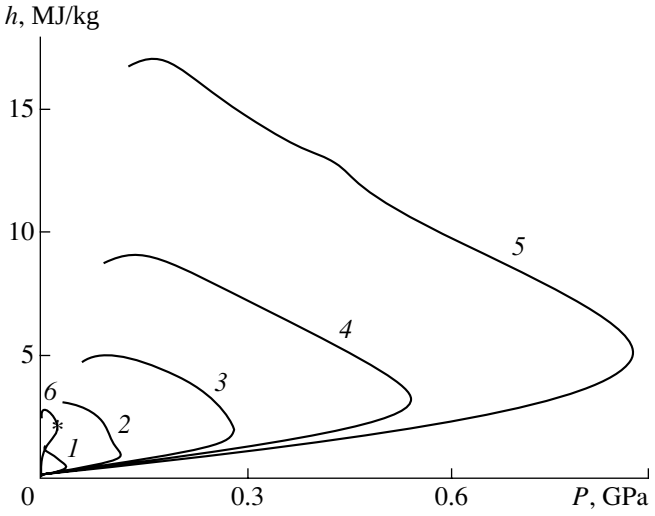

Fig. 1. Enthalpy–pressure diagram for the heating and divergence of water under the action of a laser pulse: (*1*) energy E of an incident laser pulse is 0.2; (*2*) 0.5; (*3*) 1; (*4*) 2; (*5*) 4 mJ. (*6*) Corresponds to the binodal, i.e., the boundary between the liquid and saturated vapor. Asterisk corresponds to the critical point.

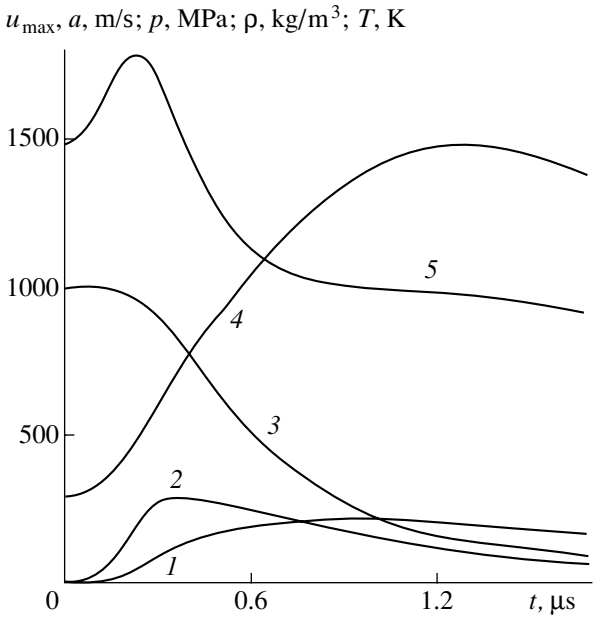

Fig. 2. Time dependences for (*1*) maximum velocity, (*2*) pressure, (*3*) density, (*4*) temperature, and (*5*) speed of sound at the laser-beam center (excluding *1*). The laser-pulse energy is E = 1 mJ.

result was verified by further dividing the steps in time and space and did not exceed 1%. The scheme of the first-order approximation was used, which allowed us to automatically calculate shock waves [6].

The diagram corresponding to heating of a thin water layer with a thickness $\Delta z = 3.0$ μm by a laser pulse with a duration of $\tau = 1.2$ μs is presented in Fig. 1. The beam's cross-sectional area is $S = 2 \times 10^{-7}$ m^2 (the exponential radius $r_0 = 2.52 \times 10^{-4}$ m). The laser-pulse energy varied within the range 0.2–4 mJ. The radiation wavelength, the absorption coefficient, and the transmission (transparency) in the unperturbed medium were $\lambda = 2.94$ μm, $\alpha = 1.28$ m^{-1}, $T_{trans,\,0} = \dfrac{E_{out}}{E} = 0.02$, respectively, where E_{out} is the laser-pulse energy at the output of the liquid layer. For analytical convenience, we have plotted the binodal (curve *6*), i.e., a liquid–saturated vapor equilibrium line. In the cases of *2–5*, the heating occurs in the supercritical regime. For variant *1*, the water–vapor phase transition is possible only in the last stage after completing the laser-pulse action. For variants *3–5*, the viscosity (and heat conduction) was higher by several orders of magnitude in order to smooth discontinuities at the shock-wave front and to provide calculation stability. In this case, the Reynolds number, the Peclet number, and the Prandtl number were, respectively, 5.2, 12.5, and 2.41. Verification of the calculation and comparison with nonviscous solution have shown that, for the transport coefficients taken by us, the values of the desired quantities, namely, of the velocity, density, and temperature, virtually do not vary.

In Fig. 2, the maximum velocity $u_{max}(t) = \max[u(r, t)]$, pressure p, density ρ, temperature T, and the speed of sound a in the beam center ($r = 0$) are presented as a function of time. The absolute maximum of the velocity u_{max} is attained at the last quarter of the laser pulse, while the maximum of pressure and of the speed of sound are attained at the first quarter. The tem-

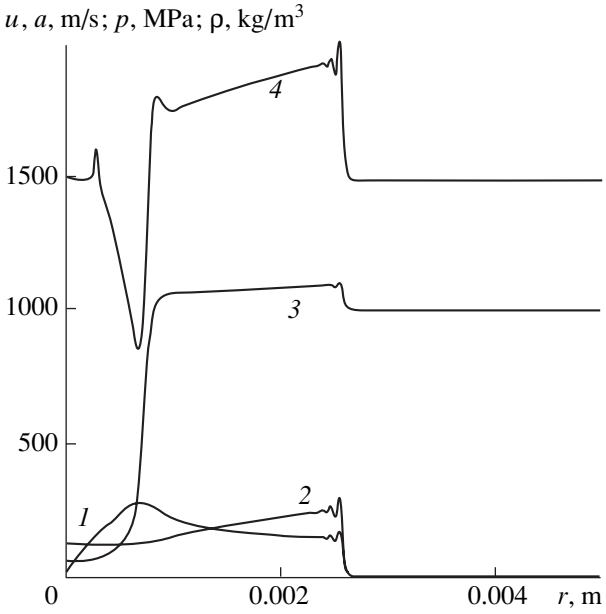

Fig. 3. Radial distributions for (*1*) velocity, (*2*) pressure, (*3*) density, and (*4*) speed of sound. The laser-pulse energy is E = 4 mJ, t = 1.439 μs.

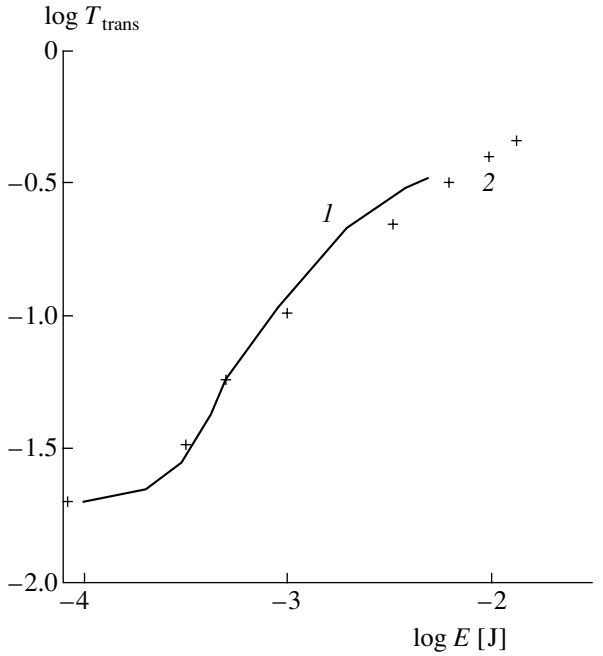

Fig. 4. Transmission (transparency) T_{trans} of water as a function of the energy E of the incident laser pulse: (*1*) numerical solution, (*2*) experimental data of [3] (giant pulse).

perature maximum is observed near the end of the laser pulse. The density of the liquid also continues to decrease after completion of the laser pulse.

In the table, maximum values of pressure, temperature, speed of sound (at the beam center), and velocity of the liquid are given for corresponding moments of time. As was indicated above, the temperature reaches its maximum at the moments $t \sim \tau$.

Radial distributions of the velocity u, pressure p, density ρ, and speed of sound a are shown in Fig. 3. The temperature sharply drops from the center to the edge of the funnel, corresponding to the shape of the density function. The temperature variations attain several degrees centigrade.

Figure 4 displays the radiation transmission $T_{trans} = \frac{E_{out}}{E}$ as a function of the laser-pulse energy E (curve *1*, 0.08 mJ ≤ E ≤ 6 mJ):

$$T_{trans} = \int_0^\infty \int_0^\infty f\left(\frac{t}{\tau}\right) \exp\left[-\frac{\alpha\rho(r,t)\Delta z}{\rho_0 - (r/r_0)^2}\right] \frac{2r\,dr}{r_0^2\,dt/\tau}. \qquad (2)$$

Crosses (curve *2*) mark the experimental data of [3] for a giant pulse. The agreement of the theoretical curve *1* with the experimental data *2* is quite satisfactory.

Thus, we have demonstrated that the evaporation mechanism of the formation of the bleaching channel is not realized (see Fig. 1). Under the assumption of invariant quantum mechanical properties of the liquid, we have theoretically described the hydrodynamic mechanism that explains bleaching of a strongly absorbing liquid under the action of a laser pulse. This effect is caused by the density reduction due to the divergence of the substance or by the hydrodynamic displacement of the liquid from the irradiated zone (Figs. 2 and 3). Within a laser-pulse energy range of about two orders of magnitude (0.08–6 mJ), we have shown a satisfactory correspondence between the theoretical results and available experimental data.

Maxima of pressure, temperature, and speed of sound (r = 0); the absolute maximum for the velocity of the liquid and the corresponding moments of time

E, mJ	p_{max}, MPa/t, μs	T_{max}, K	a_{max}, m s^{-1}/t, μs	u_{max}, m s^{-1}/t, μs
0.1	11.6/0.354	411	1574/0.443	7.58/0.633
0.15	20.6/0.354	469	1596/0.361	13.9/0.679
0.2	31.3/0.354	522	1615/0.328	21.8/0.744
0.3	56.1/0.354	633	1648/0.295	55.4/1.369
0.4	84.0/0.354	717	1675/0.277	107.9/1.553
0.5	114/0.354	812	1698/0.265	136.8/1.322
1	281.3/0.354	1478	1784/0.229	218.8/0.912
2	539.8/0.314	2814	1869/0.184	319.2/0.661
3	724.3/0.290	4074	1920/0.160	382.1/0.570
4	866.3/0.275	4289	1954/0.145	429.3/0.517
5	983.0/0.265	4365	1979/0.134	467.2/0.476
6	1083/0.258	4414	1999/0.127	499.5/0.460

REFERENCES

1. K. L. Vodop'yanov, L. A. Kulevskiĭ, P. P. Pashinin, and A. M. Prokhorov, Zh. Éksp. Teor. Fiz. **82**, 1820 (1982) [Sov. Phys. JETP **55**, 1049 (1982)].
2. K. L. Vodop'yanov, L. A. Kulevskiĭ, V. G. Mikhalevich, and A. M. Rodin, Zh. Éksp. Teor. Fiz. **91**, 114 (1986) [Sov. Phys. JETP **64**, 67 (1986)].
3. K. L. Vodop'yanov, Zh. Éksp. Teor. Fiz. **97**, 205 (1990) [Sov. Phys. JETP **70**, 114 (1990)].
4. K. L. Vodop'yanov, L. A. Kulevskiĭ, A. V. Lukashev, and P. P. Pashinin, Kvantovaya Élektron. (Moscow) **30**, 975 (1990).
5. S. I. Dolgaev, A. V. Simakin, and G. A. Shafeev, Kvantovaya Élektron. **32** (5), 443 (2002).
6. O. M. Belotserkovskiĭ and Yu. M. Davydov, *Large-Particles Method in Gas Dynamics* (Nauka, Moscow, 1982).
7. L. D. Landau and E. M. Lifshitz, *Course of Theoretical Physics*, Vol. 5: *Statistical Physics* (Nauka, Moscow, 1995; Pergamon, Oxford, 1980).
8. *GSSSD 98-86. Water* (Izd. Standartov, Moscow, 1986).
9. M. P. Vukalovich, S. L. Rivkin, and P. A. Aleksandrov, *Tables of Thermal and Physical Characteristics of Water and Steam* (Izd. Standartov, Moscow, 1969).
10. S. L. Rivkin, A. A. Aleksandrov, and E. A. Kremenevskaya, *Thermodynamic Data for Water and Steam* (Énergiya, Moscow, 1977).
11. S. L. Rivkin and A. A. Aleksandrov, *Thermodynamic Characteristics of Water and Steam* (Énergoatomizdat, Moscow, 1984).

Translated by G. Merzon

Doklady Physics, Vol. 48, No. 2, 2003, pp. 94–97. Translated from Doklady Akademii Nauk, Vol. 388, No. 5, 2003, pp. 620–623.

MECHANICS

Experimental Investigation of Changing the Filtration Mode in a Pool Due to a Redistribution of Stresses in the Oil-Reservoir Rock

L. A. Nazarov[1,*], L. A. Nazarova[1,*], A. N. Ryashentsev[2], N. P. Ryashentsev[†], and Corresponding Member of the RAS V. M. Fomin[2]

Received October 3, 2002

1. INTRODUCTION

Most technologies of increasing oil yield (flooding, intrapool combustion, vibration "clearing" of the critical zone, etc.) are based on mechanisms proceeding immediately in the production pool [1–5]. In particular, when analyzing the action of surface vibrators on a deposit, it is ignored that the amplitude of shifts and stresses in the covering rock mass as a rule exceeds that in the pool. Consequently, irreversible processes that additionally change mining-well yield can also arise in the reservoir rock.

The purpose of this study is the experimental justification of the mechanism proposed in [6] for increasing pool fluid yield. This mechanism is based on the local redistribution that is induced in stresses in the loaded block massif by an external action and is accompanied by a change in pressure in the pool.

2. JUSTIFICATION OF EXPERIMENTAL-BENCH PARAMETERS

As a prototype of the physical model, we chose a typical area of the vertical section in the neighborhood of the BS_6 pool of the Pravdinsk oil field such that it passes through one of the production wells. The basic characteristics of the real object are listed in the table, where (see also Fig. 1) l is the distance to the pressure well or the feed-contour size; t is the time; E and ρ are the Young's modulus and the reservoir-rock density, respectively; h is the pool thickness; m is the porosity; $\Delta p = p_l - p_0$, where p_l is the initial pool pressure and $p_0 = 0.1$ MPa is the atmospheric pressure; $\chi = \frac{K}{\mu}$, where K is the penetrability and μ is the viscosity of the fluid;

Table

1	2	3	4	5
Criteria				
l, m	400–500	$l^m = \delta l^r$	0.4	+
t, s	–	$t^m = \sqrt{\delta}\, t^r$	–	+
ρ, kg/m^3	2000	$\rho^m = \rho^r$	1800	+
Pool and fluid				
h, m	10–50	$h^m = \delta h^r$	0.05	+
m, %	20	$m^m = m^r$	22	+
Δp, MPa	20–30	$p_c^m = \delta p_c^r$	0.03	+
ρ_f, kg/m^3	850	$\rho_f^m = \delta\rho_f^r$	1000	+
$\dot{Q}$, m^3/s	$(3–12)\times10^{-4}$	$\dot{Q}^m = \delta^{5/2}\dot{Q}^r$	$\sim10^{-12}$	+
χ, m^2/(Pa s)	7×10^{-12}	$\chi^m = \sqrt{\delta}\,\chi^r$	3×10^{-13}	+
Reservoir medium				
σ_V, MPa	40	$\sigma_V^m = \delta\sigma_V^r$	0–0.05	+
E, GPa	25–40	$E^m = \delta E^r$	12	–
ε, %	0.10–0.16	$\varepsilon^m = \varepsilon^r$	$\sim10^{-4}$	–
w, m	$\sim10^{-5}$	$u^m = \delta u^r$	$\geq2\times10^{-8}$	+
d, m	50–500	$d^m = \delta d^r$	0.05	+
f, Hz	3–20	$f^m = \frac{f^r}{\sqrt{\delta}}$	100–600	+
Contact				
φ, deg	5–35	$\varphi^m = \varphi^r$	7.3	+
C, MPa	0–0.5	$C^m = \delta C^r$	2×10^{-5}	+

† Deceased.

[1] *Novosibirsk Mining Institute, Siberian Division, Russian Academy of Sciences, Krasnyĭ pr. 54, Novosibirsk, 630090 Russia*

[2] *Institute of Theoretical and Applied Mechanics, Russian Academy of Sciences, ul. Institutskaya 4/1, Novosibirsk, 630091 Russia*

* *e-mail: naz@misd.nsc.ru*

1028-3358/03/4802-0094$24.00 © 2003 MAIK "Nauka/Interperiodica"

ρ_f is the density of the fluid; Q is the well yield; $\sigma_V = \rho g(z_1 - h_1)$ is the lithostatic stress at the upper boundary of the object under consideration, where z_1 is the pool-location depth and g is the gravitational acceleration; ε is the strain; d is the block thickness (the distance between the subvertical continuity violations); w is the amplitude of the shift produced in the neighborhood of the deposit by an external action with frequency f; and φ and C are the angle of internal friction and adhesion of interblock contacts.

The first three lines of the table present the similarity criteria (geometric, kinematical, and dynamic [7, 8]) taken for developing the laboratory model and construction of the experimental installation. On the basis of these criteria, we obtained relationships between the model (superscript m) and real (r) parameters (column 3). The geometric-similarity ratio ($\delta = 0.001$) is chosen so that blocks B_k (Fig. 1) have a reasonable weight and shift sensors D_k can detect a value of $\sim 10^{-8}$ m, because the positive effect of vibration action is achieved for $w \sim 10^{-5}$ m under natural conditions [9].

Column 4 presents the parameters of the laboratory bench. Column 5 indicates whether or not the similarity condition for the corresponding parameter is satisfied. However, the condition for E (and, thus, for ε) is not satisfied. In principle, there are artificial materials with a low Young's modulus, but they have a low Q factor. For this reason, it is impossible to realize the vibration action immediately for the model. Therefore, the blocks were fabricated from concrete with $E^m = 12$ GPa. This circumstance does not substantially affect the quantitative results, because irreversible deformations proceed in a massif primarily along interblock violations [10] for which the similarity criteria are satisfied.

3. ESTIMATE OF STRENGTH PROPERTIES OF CONTACTS AND FILTRATION CHARACTERISTICS OF THE POOL

One of the contact surfaces of blocks B_1–B_4 was made from polished glass. This material provided both the repetition of the experiment (deformation and strength properties of violations did not change for multiple shifts of blocks) and low adhesion. Quantities φ and C were quantitatively estimated in a simple auxiliary experiment. Blocks B_k and B_{k+1} were placed on each other and on the horizontal platform (lower block is fixed, the weight of the upper block is W_k^1, and the area of the contact surface is S_k), and the platform-inclination angle β was increased up to $\beta = \beta_k^1$, when the block B_k starts to move. Then, the weight of B_k was increased up to W_k^2, and we determined $\beta = \beta_k^1$, etc. As a result, we obtained the set (W_k^i, β_k^i) with $i = 1, 2, \ldots, 6$. Now, assuming that the critical shear stress τ_k at the contact between blocks B_k and B_{k+1} is related to the normal stress σ_k by the Coulomb–Mohr law $\tau_k = \sigma_k \tan\varphi_k + C_k$ and using the evident relationships $\tau_k^i = \dfrac{W_k^i \sin\beta_k^i}{S_k}$ and $\sigma_k^i = \dfrac{W_k^i \cos\beta_k^i}{S_k}$, we found the values of φ_k and C_k by the method of least squares (table, Column 4).

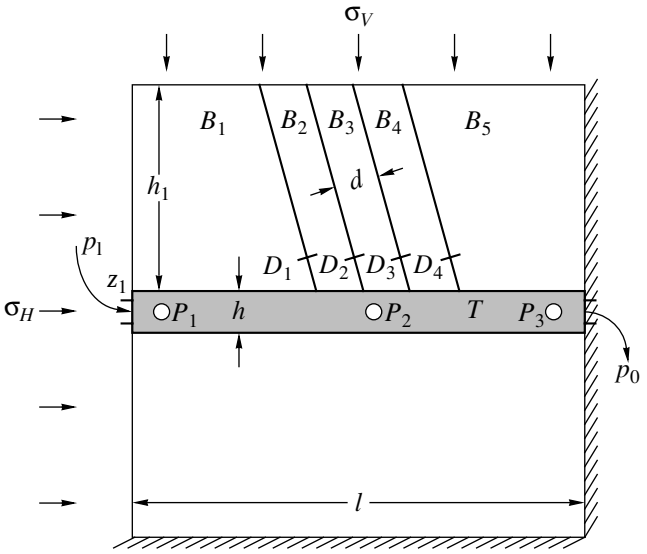

Fig. 1. Schematic diagram of the experimental bench.

The reservoir T (Fig. 1) with a volume $V = 0.003$ m^3 for the simulation of filtration processes was filled with sand ($\rho_s = 1750$ kg/m^3) so that porosity corresponded to the real value. Therefore, the necessary sand mass was $M_s = (1 - m^r)\rho_s V = 4.12$ kg. The parameter χ was estimated empirically: the constant flow rate $\dot{Q}_0$ was measured for the given pressure drop Δp in the steady-filtration mode, and we obtained $\chi = \dfrac{\dot{Q}_0 l}{s\Delta p}$, where s is the area of the outlet, from Darcy's law.

4. EXPERIMENTAL RESULTS

Each experiment involved three stages: (i) a metastable state (close to the ultimate one) with $\sigma_V^m > \sigma_H^m$ was created by choosing vertical and horizontal loads in the massif model [6]; (ii) the pool was sealed, and the inlet pressure (Fig. 1) was increased up to $p^m = p_0 + \Delta p^m$ (further, it was maintained at constant value); then, we opened the outlet orifice, waited for the onset of the steady ($\dot{Q} = \dot{Q}_0$) filtration mode, and recorded the indications of pressure sensors P_j^0; (iii) an unsteady action with a shift amplitude A (small but sufficient for

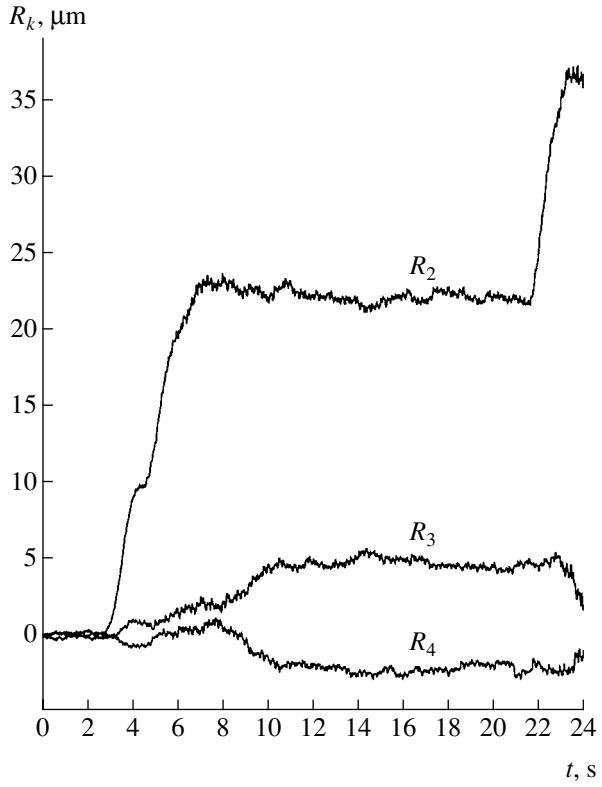

Fig. 2. Shifts of blocks when the system is disturbed from equilibrium by a vibration action with an amplitude of 0.05 μm and a frequency of 100 Hz.

converting the system into an unstable state) was applied to one of the blocks; the quantity σ_H^m was corrected (reduced as a rule) if necessary.

The instrument was switched on immediately before the onset of the unsteady action, and the relative shifts $R_k(t)$ of blocks, pressure $P_j(t)$, and flow rate $Q(t)$ were detected.

Figure 2 shows $R_k(t)$ for σ_V^m = 0.032 MPa, σ_H^m = 0.012 MPa, and Δp^m = 0.003 MPa; in this case, P_2^0 = 0.102 MPa. At time t = 3 s, we applied the action with A = 0.05 μm and frequency f^m = 100 Hz to the block B_2. Here, it is seen that blocks are shifted, and the system transits to a new state, where R_2 is more than two orders of magnitude larger than A. The slip of blocks decreases with distance from B_2: $|R_2| > |R_3| > |R_4|$; correspondingly, the effect of B_3 and B_4 on pressure in the pool decreases similarly. This corroborates the theoretical conclusion [6] that it is appropriate to initiate the shifts of the blocks immediately in the neighborhood of the deposit regions with reduced pressure.

At t = 22 s, the amplitude A increased up to 0.5 μm, which again induced a sharp change in the state of the model: R_2 increased by 12 μm. Therefore, the repeated unsteady treatment of the pool under real conditions should likely be made only once natural or artificial factors bring the massif into a metastable state that can be "disturbed" by the power of available sources.

Figure 3 shows both the relative pressure increment $\Delta\bar{P}_2(t) = \dfrac{P_2(t)}{P_2^0} - 1$ in the case of disturbing the system from equilibrium (the same static loads) by vibration action (A = 0.5 μm and f^m = 100 Hz) and relative variation in the flow rate $\Delta\bar{Q}(t) = \dfrac{Q(t)}{\dot{Q}_0(t)} - 1$. The small increment of these quantities (~5%) is retained even after vibration stops.

Figure 4 shows the distributions $\Delta\bar{P}_2(t)$ and $\Delta\bar{Q}(t)$ for the same initial experimental conditions, but when B_2 was under a vertical pulsed load with amplitude A = 0.6 μm and pulse duration $t_0 \approx 0.02$ s. In this case, the relative shift of blocks increases stepwise (corresponding to the dynamic action) rather than monotonically

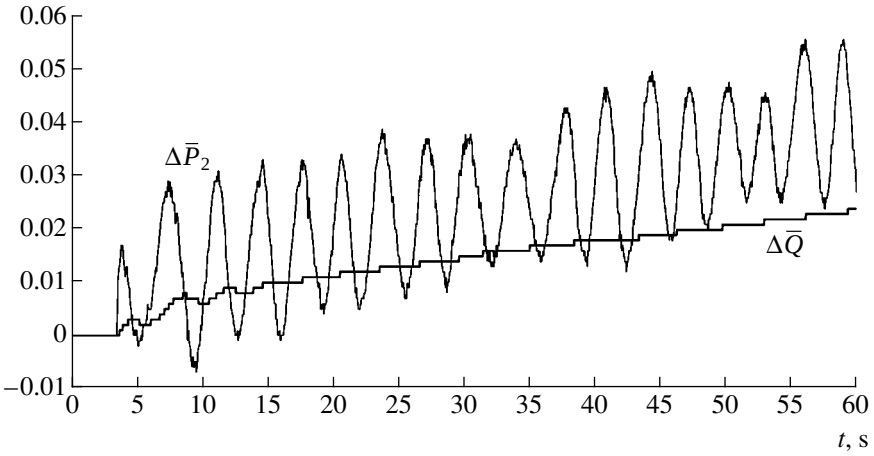

Fig. 3. Relative pressure increment and relative variation in the flow rate when the system is disturbed from equilibrium by a vibration action with an amplitude of 0.5 μm and a frequency of 100 Hz.

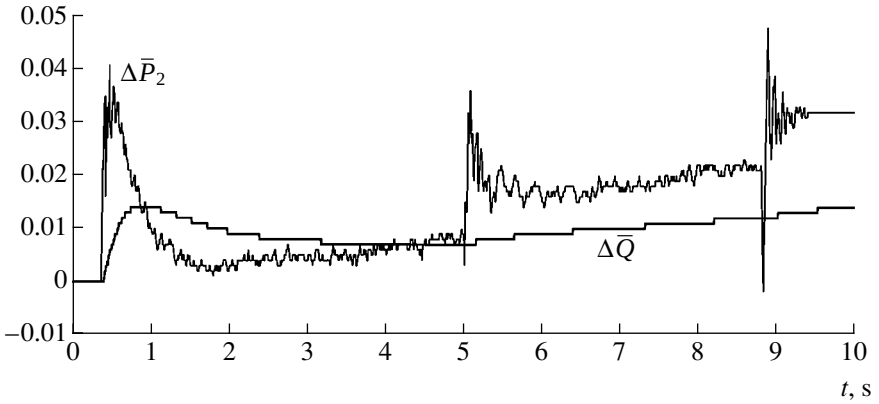

Fig. 4. Same as in Fig. 3, but under a pulsed action with an amplitude of 0.6 μm and a duration of 0.02 s.

(as in the case of vibration). The behavior of pressure in the pool is similar. We point to the pronounced aftereffect: the time of stabilization of pressure after shock load exceeds t_0 at least by an order of magnitude.

5. CONCLUSIONS

Thus, weak dynamic actions can initiate the redistribution of stresses in a block medium that is subjected to the action of quasisteady loads. As a result, the pressure in pools and fluid yield increase. In this case, the relative shifts of blocks exceed the amplitude of the external action by several orders of magnitude. This phenomenon is attributed to the release of the elastic energy accumulated by the massif.

ACKNOWLEDGMENTS

This work was supported by Schlumberger Oilfield Services, an international company in the oil and gas industry, and by the US Civilian Research and Development Foundation for the Independent States of the Former Soviet Union, contract RGO-679-A.

REFERENCES

1. G. G. Vakhitov and É. M. Simkin, *Using of Physical Fields for Oil Extraction from Pools* (Nedra, Moscow, 1985).
2. O. L. Kuznetsov, É. M. Simkin, and J. Chilingar, *Physical Principles of Vibration and Acoustic Influence on Oil–Gas Pools* (Mir, Moscow, 2001).
3. Yu. I. Voĭtenko, N. A. Lysyuk, V. I. Kras'ko, and L. A. Mityuk, Fiz. Tekh. Probl. Razrab. Polezn. Iskop., No. 2, 66 (2002).
4. http://www.ees4.lanl.gov/stimulation/ngotp, *Seismic Stimulation for Enhanced Production of Oil Reservoirs*.
5. S. A. Khristianovich, Yu. F. Kovalenko, Yu. V. Kulinich, and V. I. Karev, Neft Gaz, No. 2, 90 (2001).
6. L. A. Nazarov, L. A. Nazarova, A. N. Ryashentsev, *et al.*, Dokl. Akad. Nauk **382**, 41 (2002) [Dokl. Phys. **47**, 12 (2002)].
7. L. I. Sedov, *Similarity and Dimensional Methods in Mechanics* (Nauka, Moscow, 1987; Academic, New York, 1959).
8. I. A. Turchaninov, M. A. Iofis, and É. V. Kaspar'yan, *Principles of Rock Mechanics* (Nedra, Leningrad, 1977; Terraspace, Rockville, Md., 1979).
9. N. P. Ryashentsev, Yu. S. Ashchepkov, L. A. Nazarov, *et al.*, Preprint No. 31, IGD SO AN SSSR (Inst. of Rock Affair, Sib. Otd. Akad. Nauk, Novosibirsk, 1989).
10. M. A. Sadovskiĭ, L. G. Bolkhovitinov, and V. F. Pisarenko, *Deformation of a Medium and Seismic Process* (Nauka, Moscow, 1987).

Translated by V. Bukhanov

Doklady Physics, Vol. 48, No. 2, 2003, pp. 98–101. Translated from Doklady Akademii Nauk, Vol. 388, No. 6, 2003, pp. 757–760.

MECHANICS

Mechanics of Transformed Systems

V. V. Velichenko

Presented by Academician K.V. Frolov June 27, 2002

Received July 17, 2002

A general method is proposed for the description of transformed mechanical systems that change their composition and structure in motion. Laws of change in momentum and discontinuous equations of motion that describe the dynamics of holonomic, arbitrarily complex, transformed systems are derived. The equations are represented in an explicit form convenient for computer calculations.

1. INTRODUCTION

Problems requiring the study of mechanical systems that change their composition and structure constantly arise in engineering practice: problems of the docking of space vehicles and separation of rocket stages; problems concerning complex working operations of robots; dynamics of mechanisms and machines with clearances and backlashes; problems of impact in complex systems; etc. These problems are of fundamental importance for the analysis of accidents and catastrophes involving mechanical objects.

Dynamic systems with varying structure and composition were analyzed in optimal control theory [1–5]. As a result, complex problems of control of these systems can be solved in engineering practice. This experience enables one to analyze the similar problem for transformed mechanical systems.

This paper presents the foundations of the theory of transformed mechanical systems, including the principles of their description, mechanics of impact phenomena at transformation instants, analytical and computer methods of composing discontinuous equations of their motion. This theory is based on matrix-geometry methods [6–9]. The jumps of the phase coordinates at the instants of system transformation are obtained in an explicit form. For this reason, the problem of mathematical simulation of their dynamics can be solved, and the methods of optimal control theory can be applied. Some points of this work were reported in part in [10–13].

Blagonravov Institute of Mechanical Engineering, Russian Academy of Sciences, ul. Griboedova 4, Moscow, 101830 Russia
e-mail: velichenko@mtu-net.ru

2. DECOMPOSITION MODEL OF A TRANSFORMED MECHANICAL SYSTEM

A transformed mechanical system is a set of elements, blocks, units, and subsystems involved in all the processes where the system changes its composition and structure. According to [6–8], we decompose this system into blocks described by the matrix equations of motion

$$M^i\frac{d^2u^i}{dt^2} = g^i + f^i + \rho^i + F^{ij}\delta(t_j) + R^{ji}\delta(t_j), \quad \det M^i \neq 0. \tag{1}$$

Here, M^i is the mass matrix of the ith block, u^i is the vector of its coordinates, g^i is the vector of those terms of equations that do not involve the accelerations of the block, f^i is the vector of external forces applied to the block, ρ^i is the vector of reaction forces that act on the block and are induced by constraints that are cut when decomposing, F^{ji} is the vector of pulses of external forces applied to the ith block at time t_j, R^{ji} is the vector of pulsed reactions of constraints, i.e., of forces arising in the constraints of the system under transformations and pulses of external forces, and $\delta(t_j)$ is the Dirac delta function.

The equation for the whole system is the composition of Eqs. (1) for its blocks:

$$M\frac{d^2u}{dt^2} = g + f + \rho + F^j\delta(t_j) + R^j\delta(t_j), \quad \det M \neq 0. \tag{2}$$

The block diagonal mass matrix M of the system and column vectors on the right-hand side of Eq. (2) consist of the mass matrices and column vectors of Eqs. (1) for blocks:

$$M = \operatorname{diag}[M^i]; \quad u = \operatorname{vect}[u^i],\ g = \operatorname{vect}[g^i],\ \ldots,\ R^j = \operatorname{vect}[R^{ji}]. \tag{3}$$

In the decomposition representation, any transformation of mechanical system (2) can be described by

1028-3358/03/4802-0098$24.00

the scenarios of change in the composition of imposed mechanical constraints:

$$\xi^j(u, t) = 0, \quad \dim\xi^j = d_j, \quad t \in (t_j, t_{j+1}), \quad j = 1, 2, \ldots, J. \tag{4}$$

The column vector ξ^j consists of the set of constraints ξ^j_k that are imposed on system (2) at time t_j and are substituted for the constraint vector ξ^{j-1} generally having other dimensionality and other components ξ^{j-1}_l. If certain components of the constraint vector ξ^{j-1} are conserved under the transformation of the system, they are included in the constraint vector ξ^j.

In geometric terms, Eqs. (4) describe the set of the configuration manifolds of the system S^j in its coordinate space U. The vector of the system coordinates u moves along these manifolds, which generally have different dimensionalities. As manifolds S^j change, the number of degrees of freedom and the composition of the generalized coordinates of the system change too.

The decomposition description provides the possibility of analyzing system (2)–(4) by means of the coordinate vector u conserving its dimensionality and the composition of the components.

In decomposition description [6–8], the geometric analysis of mechanical systems is primarily based on normal fiber bundles N^j of configuration manifolds S^j and their local bases

$$K^j = \left[\frac{\partial\xi^j_1}{\partial u}\ \frac{\partial\xi^j_2}{\partial u}\ \cdots\ \frac{\partial\xi^j_{dj}}{\partial u}\right] = \frac{\partial\xi^{j\prime}(u, t)}{\partial u}, \quad \operatorname{rank}K^j = d_j. \tag{5}$$

Hereafter, the prime means transposition.

We consider ideal constraints (4) and corresponding smooth manifolds S^j acting on system (2) through the reaction vectors ρ^j and R^j, which are normal to S^j and can be decomposed into the orts of the bases K^j:

$$\rho^j \in N^j, \quad \rho^j = K^j\lambda^j; \quad R^j \in N^j, \quad R^j = K^j\Lambda^j. \tag{6}$$

3. MECHANICAL LAWS OF TRANSFORMED SYSTEMS

We consider a regular case, where the scenario of transformations of system (2) consists of a sequence of sections where motion is continuous and between which constraints (4) change instantaneously. External-force pulses F^j can be applied to the system simultaneously with its transformations. It is assumed that pulses F^j are not involved in the removal of the constraints ξ^{j-1} and interact only with the constraints ξ^j; i.e., $F^j = F^j(t_j + 0)$.

3.1. Discontinuous Change in the Momentum under the Transformations of a Mechanical System

Theorem 1. *When system* (2) *transforms its constraints* (4) *and is simultaneously exposed to external force pulses F^j, the momentum $Q = Mv$ of the system is discontinuous at the time of transformation*:

$$\begin{aligned}\Delta Q &= Mv(t_j + 0) - Mv(t_j - 0)\\ &= -K^j(K^{j\prime}M^{-1}K^j)^{-1}K^{j\prime}v(t_j - 0)\\ &+ [I - K^j(K^{j\prime}M^{-1}K^j)^{-1}K^{j\prime}M^{-1}]F^j\\ &- K^j(K^{j\prime}M^{-1}K^j)^{-1}\frac{\partial\xi^j(u, t_j)}{\partial t_j}.\end{aligned} \tag{7}$$

At the instant of transformation, imposed constraints (4) *act on the system through the impact pulse of reaction forces*:

$$R^j = -K^j(K^{j\prime}M^{-1}K^j)^{-1} \times\left[K^{j\prime}v(t_j - 0) + K^{j\prime}M^{-1}F^j - \frac{\partial\xi^j}{\partial t_j}\right]. \tag{8}$$

Generalized law (7) of change in momentum involves the classical laws of change and conservation of momentum and moment of momentum of the mechanical system in the cases where they are applicable to problems of the transformation of the system. These classical laws are insufficient for the solution of nontrivial transformation problems solved with law (7).

3.2. Discontinuous Equation of Motion of the Transformed Mechanical System

Theorem 2. *The motion of the transformed mechanical system given by Eqs.* (2) *and* (4) *is determined by the differential equations*

$$\frac{d^2u}{dt^2} = M^{-1}\left\{[I - K^j(K^{j\prime}M^{-1}K^j)^{-1}K^{j\prime}M^{-1}](f + g) - K^j(K^{j\prime}M^{-1}K^j)^{-1}\left[\left(\frac{dK^{j\prime}}{dt} + \frac{\partial K^{j\prime}}{\partial t}\right)v + \frac{\partial^2\xi^j(u, t)}{\partial t^2}\right]\right\}, \quad t \in (t_j, t_{j+1}); \tag{9}$$

and the system coordinates u at the transformation instants t_j are continuous,

$$u(t_j + 0) = u(t_j - 0),$$

whereas velocities are discontinuous,

$$v(t_j + 0) = [I - M^{-1}K^j(K^{j\prime}M^{-1}K^j)^{-1}K^{j\prime}] \times [v(t_j - 0) + M^{-1}F^j] - M^{-1}K^j(K^{j\prime}M^{-1}K^j)^{-1}\frac{\partial \xi^j(u, t_j)}{\partial t_j}. \quad (10)$$

Theorems are proved by solving the set of Eqs. (2), (4), and (6) by matrix methods [6–8]. The resulting solutions (7)–(10) are unique.

Explicit Eqs. (9) and (10) reduce the construction of a mathematical model of motion for transformed systems to standard matrix operations. These operations provide algorithms for computer programs for solving complex problems.

4. EXAMPLES

We illustrate the method with two examples.

Example 1. Rigid bodies with masses m_1 and m_2 and moments of inertia J_1 and J_2 move in a plane with given linear velocities v_{1x}^-, v_{1y}^-, v_{2x}^-, and v_{2y}^- and angular velocities ω_1^- and ω_2^-, come into contact with each other, and continue to move while engaged at the contact point. It is necessary to determine the linear and angular velocities of the bodies after contact.

Known impact theories [14, 15] provide various methods of composing equations that must be solved. In contrast, equalities (8) and (10) provide the final solution to the problem in the general formulation in arbitrarily complex systems of any composition.

Solution. We direct the abscissa axes of coupled central coordinate systems of the bodies to the contact point. Let h_1 and h_2 be the distances from the centers of mass to the contact point.

Decomposing the system into individual bodies, we write equations of its motion (2) as

$$m_1\frac{d^2x_1}{dt^2} = f_{1x} + R_{1x}, \quad m_2\frac{d^2x_2}{dt^2} = f_{2x} + R_{2x},$$
$$m_1\frac{d^2y_1}{dt^2} = f_{1y} + R_{1y}, \quad m_2\frac{d^2y_2}{dt^2} = f_{2y} + R_{2y}, \quad (E.1)$$
$$J_1\frac{d^2\varphi_1}{dt^2} = f_{1\varphi} + R_{1\varphi}, \quad J_2\frac{d^2\varphi_2}{dt^2} = f_{2\varphi} + R_{2\varphi}.$$

The mass matrix and coordinate vector (3) of system (E.1) have the form

$$M = \mathrm{diag}[m_1\ m_1\ J_1\ m_2\ m_2\ J_2], \quad u' = [x_1\ y_1\ \varphi_1\ x_2\ y_2\ \varphi_2]. \quad (E.2)$$

The vector of constraints (4) imposed at the contact of the bodies has the form

$$\xi = \begin{bmatrix}\xi_1\\ \xi_2\end{bmatrix} = \begin{bmatrix}x_1 + h_1\cos\varphi_1 - x_2 - h_2\cos\varphi_2\\ y_1 + h_1\sin\varphi_1 - y_2 - h_2\sin\varphi_2\end{bmatrix} = 0. \quad (E.3)$$

Differentiating column vector ξ (E.3) with respect to row vector u' (E.2), we obtain the transposed matrix of the normal basis

$$K' = \frac{\partial \xi}{\partial u'} = \begin{bmatrix}1 & 0 & -h_1\sin\varphi_1 & -1 & 0 & h_2\sin\varphi_2\\ 0 & 1 & h_1\cos\varphi_1 & 0 & -1 & -h_2\cos\varphi_2\end{bmatrix}. \quad (E.4)$$

Using matrices M (E.2) and K (E.4), we calculate the following 36-element matrix of the transformation of velocities from Eq. (10):

$$W_{vv} = I - M^{-1}K(K'M^{-1}K)^{-1}K' = \Delta^{-1}\begin{bmatrix}\Delta - m_1^{-1}B & -m_1^{-1}C & m_1^{-1}a & m_1^{-1}B & m_1^{-1}C & -m_1^{-1}c\\ -m_1^{-1}C & \Delta - m_1^{-1}A & m_1^{-1}b & m_1^{-1}C & m_1^{-1}A & -m_1^{-1}d\\ J_1^{-1}a & J_1^{-1}b & \Delta - J_1^{-1}e & -J_1^{-1}a & -J_1^{-1}b & J_1^{-1}g\\ m_2^{-1}B & m_2^{-1}C & -m_2^{-1}a & \Delta - m_2^{-1}B & -m_2^{-1}C & m_2^{-1}c\\ m_2^{-1}C & m_2^{-1}A & -m_2^{-1}b & -m_2^{-1}C & \Delta - m_2^{-1}A & m_2^{-1}d\\ -J_2^{-1}c & -J_2^{-1}d & J_2^{-1}g & J_2^{-1}c & J_2^{-1}d & \Delta - J_2^{-1}k\end{bmatrix}. \quad (E.5)$$

Here,

$$\Delta = AB - C^2,$$
$$A = m_1^{-1} + m_2^{-1} + J_1^{-1}h_1^2\sin^2\varphi_1 + J_2^{-1}h_2^2\sin^2\varphi_2,$$
$$B = m_1^{-1} + m_2^{-1} + J_1^{-1}h_1^2\cos^2\varphi_1 + J_2^{-1}h_2^2\cos^2\varphi_2,$$
$$C = J_1^{-1}h_1^2\sin\varphi_1\cos\varphi_1 + J_2^{-1}h_2^2\sin\varphi_2\cos\varphi_2;$$
$$a = h_1(B\sin\varphi_1 - C\cos\varphi_1),$$
$$b = h_1(C\sin\varphi_1 - A\cos\varphi_1),$$

$$c = h_2(B\sin\varphi_2 - C\cos\varphi_2),$$
$$d = h_2(C\sin\varphi_2 - A\cos\varphi_2),$$
$$e = h_1(a\sin\varphi_1 - b\cos\varphi_1),$$
$$k = h_2(c\sin\varphi_2 - d\cos\varphi_2),$$
$$g = h_1(c\sin\varphi_1 - d\cos\varphi_1)$$
$$= h_2(a\sin\varphi_2 - b\cos\varphi_2).$$

For $F = 0$ and $\frac{\partial\xi}{\partial t} = 0$, the substitution of Eq. (E.5) into Eq. (10) yields the following formula, which transforms the velocity vector v^- of the system before collision to the velocity vector v^+ after collision:

$$v^{+\prime} = [v_{1x}^+ \; v_{1y}^+ \; \omega_1^+ \; v_{2x}^+ \; v_{2y}^+ \; \omega_2^+]$$
$$= [v_{1x}^- \; v_{1y}^- \; \omega_1^- \; v_{2x}^- \; v_{2y}^- \; \omega_2^-]W'_{vv}. \qquad \text{(E.6)}$$

In particular, the velocity components v_{1x}^+ and v_{2x}^+ have the form

$$v_{1x}^+ = \Delta^{-1}[(\Delta - m_1^{-1}B)v_{1x}^- - m_1^{-1}Cv_{1y}^- + m_1^{-1}a\omega_1^-$$
$$+ m_1^{-1}Bv_{2x}^- + m_1^{-1}Cv_{2y}^- - m_1^{-1}c\omega_2^-],$$
$$v_{2x}^+ = \Delta^{-1}[m_2^{-1}Bv_{1x}^- + m_2^{-1}Cv_{1y}^- - m_2^{-1}a\omega_1^-$$
$$+ (\Delta - m_2^{-1}B)v_{2x}^- - m_2^{-1}Cv_{2y}^- + m_2^{-1}c\omega_2^-].$$

For transformation (E.6) of the system under the action of only internal forces, the classical mechanical laws of the conservation of momentum and moment of momentum are valid. However, these laws are insufficient to determine the six desired components of the vector v^+. This transformation involves additional independent laws for the velocities of the system. These laws are explicitly given by 6-dimensional vector formulas (10) and (E.5), where they are represented in the computational interpretation rather than in the informative form as classical laws.

Example 2. In the problem of docking in the spatial formulation, formula (10) determines the transformation of the 12 linear and angular velocities of the bodies before docking and 12 velocities after docking. Correspondingly, transformation matrix (E.5) changes to a 12×12 matrix whose 144 elements are easily calculated on a computer, but it is difficult to write them on paper.

Transformation problems for arbitrarily complex systems are solved similarly. Computer numerical calculations by explicit formulas (7)–(10) are elementary for any problem. An analytical solution faces problems, because it is impossible to write computer solutions on paper due to enormous formula information.

ACKNOWLEDGMENTS

I am grateful to V.S. Syromyatnikov for the formulation of problems of the docking dynamics of space vehicles, which stimulated this work.

REFERENCES

1. L. S. Pontryagin, V. G. Boltyanskiĭ, R. V. Gamkrelidze, and E. F. Mishchenko, *The Mathematical Theory of Optimal Processes* (Nauka, Moscow, 1983; Gordon and Breach, New York, 1986).
2. V. V. Velichenko, Avtom. Telemekh., No. 7, 20 (1966).
3. V. V. Velichenko, Dokl. Akad. Nauk SSSR **176**, 754 (1967).
4. V. V. Velichenko, Dokl. Akad. Nauk **350**, 9 (1996).
5. V. V. Velichenko, Theory Appl. **30** (4), 2065 (1997).
6. V. V. Velichenko, *Matrices, Geometry, Mechanics, and Computers* (Mosk. Fiz.-Tekh. Inst., Moscow, 1984).
7. V. V. Velichenko, Dokl. Akad. Nauk SSSR **285**, 1340 (1985).
8. V. V. Velichenko, *Matrix-Geometry Methods in Mechanics with Application to Problems of Robotics* (Nauka, Moscow, 1988).
9. V. V. Velichenko, Dokl. Akad. Nauk SSSR **321**, 499 (1991).
10. V. V. Velichenko, in *Proceedings of the International Congress on Nonlinear Analysis and its Applications, Moscow, 1998*, p. 107.
11. V. V. Velichenko, in *Proceedings of the XII Symposium on Dynamics of Vibro-Impact (Strong-Nonlinear) Systems, Moscow, 1998*, p. 62.
12. V. V. Velichenko, in *Proceedings of the XII Baĭkal Conference, Irkutsk, 2001*, p. 62.
13. V. V. Velichenko, in *Proceedings of the VIII All-Russia Congress on Theoretical and Applied Mechanics, Perm, 2001*, p. 149.
14. G. K. Suslov, *Theoretical Mechanics* (Gostekhizdat, Moscow, 1944).
15. L. A. Pars, *Treatise on Analytical Dynamics* (Wiley, New York, 1965; Nauka, Moscow, 1971).

Translated by R. Tyapaev